SANDIA REPORT

SAND98—8231 • UC—411
Unlimited Release
Printed February 1998

Modeling Electrodeposition for LIGA Microdevice Fabrication

S. K. Griffiths, R. H. Nilson, R. W. Bradshaw, A. Ting,
W. D. Bonivert, J. T. Hachman, J. M. Hruby

RECEIVED
MAR 3 0 1998
OSTI

Prepared by
Sandia National Laboratories
Albuquerque, New Mexico 87185 and Livermore, California 94550

Sandia is a multiprogram laboratory operated by Sandia Corporation, a Lockheed Martin Company, for the United States Department of Energy under Contract DE-AC04-94AL85000.

DISTRIBUTION OF THIS DOCUMENT IS UNLIMITED

Approved for public release; distribution is unlimited.

MASTER

Sandia National Laboratories

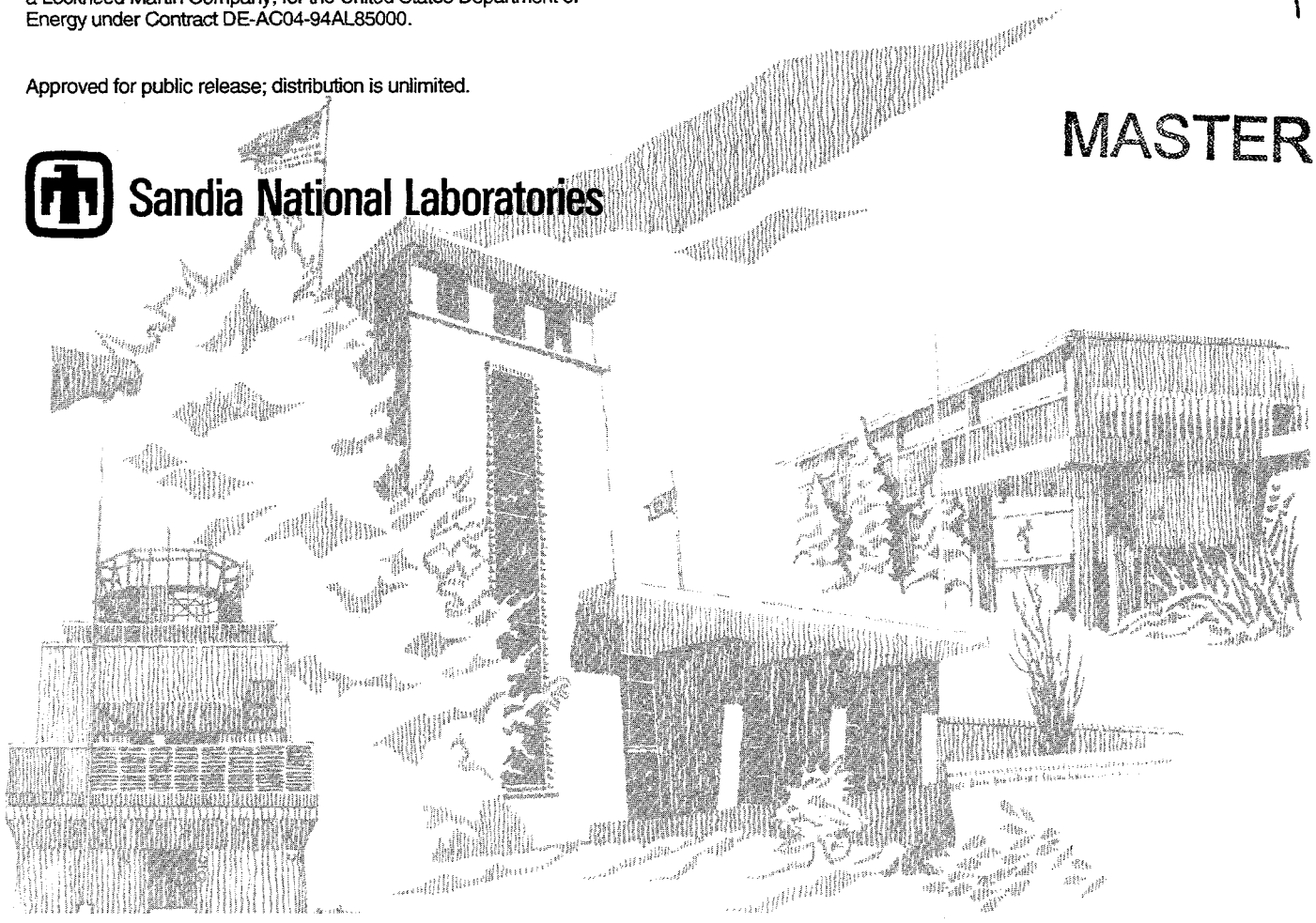

Issued by Sandia National Laboratories, operated for the United States Department of Energy by Sandia Corporation.
NOTICE: This report was prepared as an account of work sponsored by an agency of the United States Government. Neither the United States Government nor any agency thereof, nor any of their employees, nor any of their contractors, subcontractors, or their employees, makes any warranty, express or implied, or assumes any legal liability or responsibility for the accuracy, completeness, or usefulness of any information, apparatus, product, or process disclosed, or represents that its use would not infringe privately owned rights. Reference herein to any specific commercial product, process, or service by trade name, trademark, manufacturer, or otherwise, does not necessarily constitute or imply its endorsement, recommendation, or favoring by the United States Government, any agency thereof, or any of their contractors or subcontractors. The views and opinions expressed herein do not necessarily state or reflect those of the United States Government, any agency thereof, or any of their contractors.

Printed in the United States of America. This report has been reproduced directly from the best available copy.

Available to DOE and DOE contractors from
Office of Scientific and Technical Information
P.O. Box 62
Oak Ridge, TN 37831

Prices available from (615) 576-8401, FTS 626-8401

Available to the public from
National Technical Information Service
U.S. Department of Commerce
5285 Port Royal Rd
Springfield, VA 22161

NTIS price codes
Printed copy: A03
Microfiche copy: A01

DISCLAIMER

Portions of this document may be illegible electronic image products. Images are produced from the best available original document.

SAND98-8231
Unlimited Release
Printed February 1998

Distribution
Category UC-411

Modeling Electrodeposition for LIGA Microdevice Fabrication

S. K. Griffiths, R. H. Nilson, R. W. Bradshaw
A. Ting, W. D. Bonivert, J. T. Hachman and J. M. Hruby
Sandia National Laboratories
Livermore, California 94551-0969

Abstract

To better understand and to help optimize the electroforming portion of the LIGA process, we have developed one and two-dimensional numerical models describing electrodeposition of metal into high aspect-ratio molds. The one-dimensional model addresses dissociation, diffusion, electromigration, and deposition of multiple ion species. The two-dimensional model is limited to a single species, but includes transport induced by forced flow of electrolyte outside the mold and by buoyancy associated with metal ion depletion within the mold. To guide model development and to validate these models, we have also conducted a series of laboratory experiments using a sulfamate bath to deposit nickel in cylindrical molds having aspect ratios up to twenty-five. The experimental results indicate that current densities well in excess of the diffusion-limited currents may still yield metal deposits of acceptable morphology. However, the numerical models demonstrate that such large ion fluxes cannot be sustained by convection within the mold resulting from flow across the mold top. Instead, calculations suggest that the observed enhancement of transport probably results from natural convection within the molds, and that buoyancy-driven flows may be critical to metal ion transport even in micron-scale features having very large aspect ratios. Taking advantage of this enhanced ion transport may allow order-of-magnitude reductions in electroforming times for LIGA microdevice fabrication.

This Page Intentionally Left Blank

Introduction

LIGA, an acronym from the German words for lithography, electroforming and molding, is a promising new process for producing high aspect-ratio metal microdevices having micron to millimeter features [1,2,3]. In LIGA, high-energy x-ray lithography is used to produce a deep non-conducting mold [4,5,6] that is subsequently filled by means of electrodeposition to produce metal parts. The final step in true LIGA is injection molding for mass production, here using the electroformed metal part as a mold. Currently under worldwide development, this process offers a means to manufacture high resolution, high aspect-ratio devices including microscale valves, motors, solenoid actuators, and gear trains [7-10]. Such devices cannot be fabricated either by silicon micromachining or by precision machine tool operations.

Most previous research in LIGA has focused on lithography and developing [4-6,11,12]. Electrodeposition for LIGA has been relatively neglected, despite several serious problems. Large-scale voids in the deposited metal occur frequently and often without apparent cause. Similarly, local deposition rates within a mold vary widely depending on local feature sizes and on the macro-scale geometry of collections of features. Such local variations in deposition rate lead to uneven mold filling and, eventually, to regions of the mold that cannot be filled completely. Further, deposition surfaces are often rough or wavy, necessitating post-deposition polishing to produce parts having acceptable tolerances and surface finish. These problems are due in part to the depletion of metal ions and the accumulation of hydrogen in the layer between the top and bottom of the mold [13,14]. The presence of this layer distinguishes electrodeposition for LIGA from all traditional electroplating and electroforming processes. As a result, traditional electroplating practices have not proven very effective in filling the deep holes and trenches characteristic of LIGA molds.

Many of these problems likely result from transport limitations that arise because the electrolyte in deep mold features may remain nearly stagnant, even despite vigorous bath stirring. In such a transport-limited growth process, the deposition surface will typically roughen and become unstable as deposition rates are increased and ion depletion becomes significant. Hydrogen gases may also be generated when ion depletion is significant, leading to a second mechanism for anomalies in the deposition surface. Although it may be possible to avoid these nonuniformities by reducing deposition rates, the electroforming portion of the LIGA process presently may require days or even weeks. Thus further reducing deposition rates may become burdensome to overall LIGA processing cost and cycle time. In addition, the very low overpotentials associated with low current densities and low deposition rates may themselves produce unacceptable metal morphologies.

To help understand these problems and to help optimize the process, we have developed a pair of numerical models. The first is a one-dimensional model describing the electric field and diffusion, dissociation, electromigration, and the deposition kinetics of multiple ion species. This model is used to compute spatial variations in ion concentrations, local pH and associated surface deposition rates based on bath chemistry, mold geometry and applied current for cases in which electrolyte within the feature may be considered stagnant. Both steady and transient solutions can be computed

using this multi-species model. The second is quasi-steady two-dimensional model addressing forced and buoyancy-driven convection, as well as diffusion, outside and within the mold. This second model considers only a single species, but includes deposition kinetics of a form similar to those of the multi-species model. Together, these two models address all key physics of the electrodeposition of metal into high aspect-ratio molds.

In parallel with model development, we have also conducted a series of laboratory experiments. These experiments were designed to provide well characterized boundary conditions in order to obtain both qualitative and quantitative insight into the transport processes inside mold features. By observing the deposit morphology for various mold depths, aspect ratios and plating currents, these experimental results have identified the acceptable operating conditions for nickel deposition from a sulfamate bath. Comparison of these observations with our numerical results has helped to guide model development and to validate the numerical results. This combined experimental and numerical approach has revealed that buoyancy-driven ion transport can enhance deposition rates by an order-of-magnitude or more relative to those possible by diffusion alone.

Governing Equations: Multi-Species Transport

To model electrodeposition in LIGA molds, we consider the simplified geometry of a single mold feature as shown in Fig. 1. Far from the mold top, $y \gg h$, species concentrations are at uniform values and the fluid moves with a uniform speed from left to right. This uniform far-field flow produces a linear gradient of the fluid speed in a boundary layer just above the mold top and upstream of the feature. The shear along the mold top is transmitted to the fluid at the top of the feature, and this may drive recirculating convection cells below. However, as later discussed the effects of this forced convection are negligible when the aspect ratio is large, even when fluid speeds at the mold top are also very large.

We first address the case in which buoyancy forces and the associated natural convection within the feature can be neglected. The conditions under which this is appropriate are also discussed later. In the absence of natural convection, electrodeposition inside the feature is nearly one dimensional, provided that the aspect ratio of the feature $A = h/w$ is large. For this reason, the electric field and species transport equations may be written as second-order differential equations in time and the spatial position along the mold. Species concentrations, c_i, within the feature are governed by species conservation equations [15],

$$\frac{\partial c_i}{\partial t} + \nabla \cdot \mathbf{J} = S_i \tag{1}$$

where t is time, $\mathbf{J}$ are the species fluxes, and S_i are volumetric sources or sinks associated with homogeneous reactions. Note that the concentrations c_i represent both neutral and ionic species, and that ionic species may be both metallic and nonmetallic.

The species fluxes are given by [15]

$$\mathbf{J} = -D_i \nabla c_i + e v_i z_i c_i \mathbf{E} \tag{2}$$

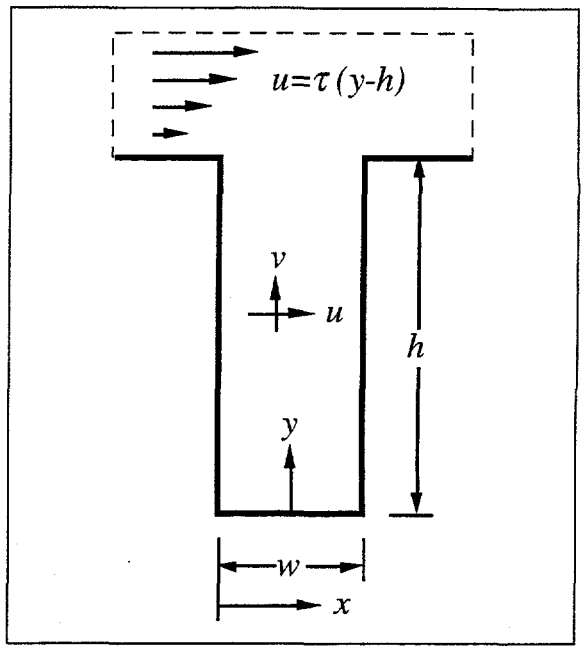

Figure 1. Schematic of a LIGA mold feature. Such a feature may be either a trench or cylinder. Metal ions are carried from the mold top to the deposition surface at the feature bottom by convection, diffusion and ion drift due to the applied electric potential. The feature aspect ratio is given by $A = h/w$.

where D_i is the effective diffusivity of the ith species, e is the elementary charge, and z_i is the species charge number. Note that the first term on the right of Eq. (2) describes ordinary diffusion of the species, while the second term describes ion drift due to the presence of the electric field. In this second term, the ion mobility, v_i, is usually approximated as

$$v_i = \frac{D_i}{kT} \tag{3}$$

where k is the Boltzmann constant, and T is the local temperature.

Recognizing that the time scale for establishing a DC electric field is much smaller than that for establishing species concentration fields, we consider here only the case of the electrostatic field. Under this restriction, and the further restriction that there are no applied magnetic fields, the electric field, $\mathbf{E}$, is governed by the Poisson equation relating the electric field to the local charge density.

$$\nabla \cdot \mathbf{E} = \frac{4\pi}{\epsilon} \sum_{i=1}^{n} e z_i c_i \tag{4a}$$

where $\mathbf{E} = -\nabla V$ is the negative of the gradient of the electric potential V, ϵ is the dielectric constant, and n is the total number of ionic species. A common alternative to solving the Poisson equation is to enforce local electroneutrality. In this case, the

electric field $\mathbf{E}$ becomes an unknown constant to be determined as part of the overall solution, and the governing equation becomes

$$\sum_{i=1}^{n} z_i c_i = 0 \tag{4b}$$

Like the Poisson equation, this condition of electroneutrality applies at every point in the concentration field, except within the Debye layer adjacent to each electrode. These regions are instead accounted for by the Butler-Volmer relations.

Consistent with the assumption of an electrostatic field, there may be no time-dependent variation in the local charge density. This is equivalent to

$$\nabla \cdot \mathbf{I} = \nabla \cdot \left(\sum_{i=1}^{n} \mathbf{I}_i \right) = \nabla \cdot \left(\sum_{i=1}^{n} z_i \mathbf{J} \right) = 0 \tag{5}$$

Currents associated with each ion species can be computed easily after the basic transport equations have been solved. These are given as the sum of the two contributions to the ion fluxes,

$$\mathbf{I}_i = F z_i \mathbf{J} = -F z_i D_i \nabla c_i + F^2 v_i z_i^2 c_i \mathbf{E} \tag{6}$$

where $\mathbf{I}_i$ is the current due to the ith species, and F is Faraday's constant. Paralleling the flux equations (2), the first term on the right of Eq. (6) is the current due to ordinary diffusion, while the second contribution results from ion drift due to the electric field acting on charged species.

Equation (5) closes the conservation equations for species and electric charge. For the case of diffusive transport considered just now, momentum equations are not required. Similarly, energy equations are everywhere replaced by an assumption that the temperature, T, is uniform and constant. In one dimension , the system of equations described above thus consists of $2n+1$ unknowns (c_i, $\mathbf{J}\cdot\mathbf{j}$, and $\mathbf{E}\cdot\mathbf{j}$) and $2n+1$ equations (2, 4a or 4b, and 5). This system of equations can in general be solved given a specified set of species, corresponding homogeneous and surface reactions, and appropriate initial and boundary conditions.

Method of Solution

To solve the governing species and field equations, we now consider a problem of the codeposition of nickel and iron from a sulfate solution. This particular codeposition process is important to LIGA in that it permits the fabrication of magnetic devices from permalloy. For this nickel-iron sulfate bath we consider eight reactive species. These are Fe^{2+}, $FeOH^{+}$, Ni^{2+}, $NiOH^{+}$, HSO_4^{-}, SO_4^{2-}, OH^{-}, and H^{+}. The H_2O concentration is assumed constant at 55 mol/ℓ. Diffusivities of these species are all about $D_i \approx 1 \times 10^{-9}$, except for the hydroxyl group for which $D_{OH^-} \approx 5 \times 10^{-9}$.

The sources or sinks in Eq. (1) arise from homogeneous reactions among these eight species. While many such reaction are possible, here we limit our attention to just the four thought to be most important. These are

$$\begin{aligned} \mathrm{Fe}^{2+} + \mathrm{OH}^- &\rightleftharpoons \mathrm{FeOH}^+ \\ \mathrm{Ni}^{2+} + \mathrm{OH}^- &\rightleftharpoons \mathrm{NiOH}^+ \\ \mathrm{H_2O} &\rightleftharpoons \mathrm{H}^+ + \mathrm{OH}^- \\ \mathrm{HSO_4^-} &\rightleftharpoons \mathrm{H}^+ + \mathrm{SO_4^{2-}} \end{aligned} \tag{7}$$

Equilibrium constants for these four reactions are about [16] $c_{\mathrm{FeOH}^+}/c_{\mathrm{Fe}^{2+}}c_{\mathrm{OH}^-} = K_{\mathrm{Fe}} \approx 3.2 \times 10^4\ \mathrm{M}^{-1}$, $c_{\mathrm{NiOH}^+}/c_{\mathrm{Ni}^{2+}}c_{\mathrm{OH}^-} = K_{\mathrm{Ni}} \approx 1.3 \times 10^4\ \mathrm{M}^{-1}$, $c_{\mathrm{H}^+}c_{\mathrm{OH}^-}/c_{\mathrm{H_2O}} = K_{\mathrm{H_2O}} \approx 1.0 \times 10^{-14}$ M, and $c_{\mathrm{H}^+}c_{\mathrm{SO_4^{2-}}}/c_{\mathrm{HSO_4^-}} = K_{\mathrm{HSO_4^-}} \approx 1.3 \times 10^{-2}$ M. Note that use of the right hand portion of these expressions does not necessarily imply equilibrium of the homogeneous reactions, provided that equilibrium constants are interpreted simply as the ratio of the forward and reverse reaction rates. In that case, either the forward or reverse rate must also be specified, and the remaining rate is then determined by the equilibrium constant.

Cathode reactions at the electrodeposition surface will generally involve both the doubly-charged metal ions and the singly-charged metal hydroxides. These reactions can be expressed as

$$\mathrm{M}^{2+} + 2e \rightarrow \mathrm{M} \tag{8}$$

for the bare metal ions, and

$$2\,\mathrm{MOH}^+ + 2e \rightarrow \mathrm{M} + \mathrm{OH}^- \tag{9}$$

for the hydroxides. Here, M represents any metallic species. All other species are considered to be inert with regard to cathode reactions, with the exception of hydrogen. Hydrogen is involved in two cathode reactions. The first is the formation of hydrogen gas from the protium cation,

$$2\,\mathrm{H}^+ + 2e \rightarrow \mathrm{H_2} \tag{10}$$

while the second is the dissociation of water,

$$2\,\mathrm{H_2O} + 2e \rightarrow \mathrm{H_2} + 2\,\mathrm{OH}^- \tag{11}$$

to form hydrogen gas and a hydroxyl radical.

The rates associated with these fundamental reactions can all be expressed in terms of the local potential, V, and local ion species concentrations, c_i. Fluxes at the cathode surface, $y = 0$, are given by [17,18]

$$J_i = a_i c_i e^{-\alpha_i F(V - V_i)/RT} \tag{12}$$

$$V_i = V_{0i} + \frac{RT}{Fz_i} \ln\left(\frac{c_i}{c_{0i}}\right) \tag{13}$$

where $J_i = \mathbf{J}\cdot\mathbf{j}$, a_i is the pre-exponential rate constant, α_i is the charge separation constant, and V_{0i} and c_{0i} are the reference potential and reference concentration, respectively. These rate relations are commonly known as the Butler-Volmer kinetic equations. Values of the constants in these equations are widely reported [17,18]. As discussed later, however, there are very large uncertainties in these values.

The special case of the governing transport equations we are considering here is when the fluid velocity everywhere within the feature is zero. This approximation is widely used in models of traditional electroplating. For that purpose, the height of the stagnant diffusion layer is equal to the diffusion boundary layer thickness. However, under a significant range of conditions, this approximation is likewise applicable to ion transport within deep LIGA features, and in this case the diffusion height is equal to the mold thickness. Further, growth of the deposition surface in all electroplating processes takes place on a time scale very long compared to the relaxation time of the ion concentration fields. Because of this, the time derivatives in the species conservation equations may be neglected when the applied electric potential is time invariant.

Under these restrictions, the transport equations (1) and (2) may be rearranged to give,

$$\frac{\partial}{\partial y}\left(J_{Fe^{2+}} + J_{FeOH^{+}}\right) = 0 \tag{14}$$

$$\frac{\partial}{\partial y}\left(J_{Ni^{2+}} + J_{NiOH^{+}}\right) = 0 \tag{15}$$

$$\frac{\partial}{\partial y}\left(J_{H^{+}} + J_{OH^{-}} + J_{HSO_4^{-}} + J_{FeOH^{+}} + J_{NiOH^{+}}\right) = 0 \tag{16}$$

These forms of the conservation equations are useful in that each equation is directly related to the partial current density of a single elemental species. Under the restrictions above, the partial currents for iron, nickel and hydrogen are

$$\mathbf{I}_{Fe}\cdot\mathbf{j} = 2F\left(J_{Fe^{2+}} + J_{FeOH^{+}}\right) \tag{17}$$

$$\mathbf{I}_{Ni}\cdot\mathbf{j} = 2F\left(J_{Ni^{2+}} + J_{NiOH^{+}}\right) \tag{18}$$

and

$$\mathbf{I}_{H_2}\cdot\mathbf{j} = F\left(J_{H^{+}} + J_{OH^{-}} + J_{HSO_4^{-}} + J_{FeOH^{+}} + J_{NiOH^{+}}\right) \tag{19}$$

These three partial currents are of practical importance because they are directly related to the deposition rates of nickel and iron and to the rate of hydrogen generation. The latter is important when ion fluxes are comparable to the diffusion limited ion transport rates since hydrogen that cannot be diffused from the cathode surface will lead to hydrogen bubble formation. Hydrogen bubbles that do not detach from the cathode give rise to poor morphology of the deposited metal. Moreover, even high concentrations of hydrogen may lead to poor metal properties as hydrogen may become entrapped in the metal during the deposition process.

This system of equations is implicitly coupled through the homogeneous dissociation reactions and through either the Poisson equation or local electroneutrality condition. The resulting system of differential equations and algebraic constraints can be integrated

numerically using DASSL [19], a stiff ODE and algebraic solver specifically intended for problems of this type. Integration is begun from the top of the mold using bath concentrations that satisfy the equilibrium dissociation relations and the electroneutrality condition. A multi-parameter shooting technique is then employed to satisfy the mixed boundary conditions at the deposition surface. The three shooting parameters are the nickel and iron partial currents and the cathode potential, V; the three targets are the total current and the two the Butler-Volmer equations relating the ion fluxes to the ion concentrations for the iron and nickel species. This technique is useful when solving problems in which the total current is specified. Alternatively, the problem may be solved without shooting by specifying a cathode potential; in this case the unknown partial and total currents are computed after the ion concentrations have been determined.

This second technique is also employed when solving the time-dependent transport problem. Such problems arise in computing usable duty cycles for pulsed plating. Pulsed plating appears to offer significant advantages for LIGA electrodeposition because peak currents may be large enough to obtain acceptable morphologies, while the mean or time-averaged current is small enough to avoid ion transport limitations and the accompanying ion depletion at the deposition surface. In the solution method for transient problems, the governing ion transport equations (1), (2) and (4) are spatially discretized on a grid of m points, as is the Poisson equation. This leads to a set of $m(n+1)$ coupled time-dependent equations where mn equations represent the ion concentrations. The remaining m equations represent the electric field. DASSL is again used to solve the coupled system of equations. In this transient case, however, the homogeneous reactions need not be in equilibrium. For problems in which the forward or reverse reaction rates are known in addition to the equilibrium constants, the forward and reverse reaction rates may be treated explicitly as either sources or sinks in Eq. (1).

Sample Calculations: Multi-Species Transport

Numerical results are shown in Fig. 2 for the codeposition of nickel and iron from a 0.5 M $NiSO_4$ and 0.1 M $FeSO_4$ bath at a pH of 3. The height of the mold is 100 μm. As this problem was previously solved by Grande and Talbot [16], it serves as a check of our numerical calculations. Figure 2 displays computed ion species concentrations for a 100 μm deep mold at a total current of 400 A/m^2. This result shows that hydroxide species concentrations increase dramatically from the bath through the mold thickness when currents are large, even though the total nickel and iron concentrations do not show significant depletion. Thus hydrogen bubble formation may also occur before any noticeable decline in deposition efficiency. Moreover, because metals may be deposited either from the bivalent metal ions or from hydroxides of the metallic species, this increase in hydroxide concentrations may alter the composition and morphology of the deposited material.

The results of Fig. 2 agree well with those of Grande and Talbot. As their analysis did not include ion drift due to the electric field, this observation confirms that ion drift is not very important in this sample problem. Having examined a broad range of problems,

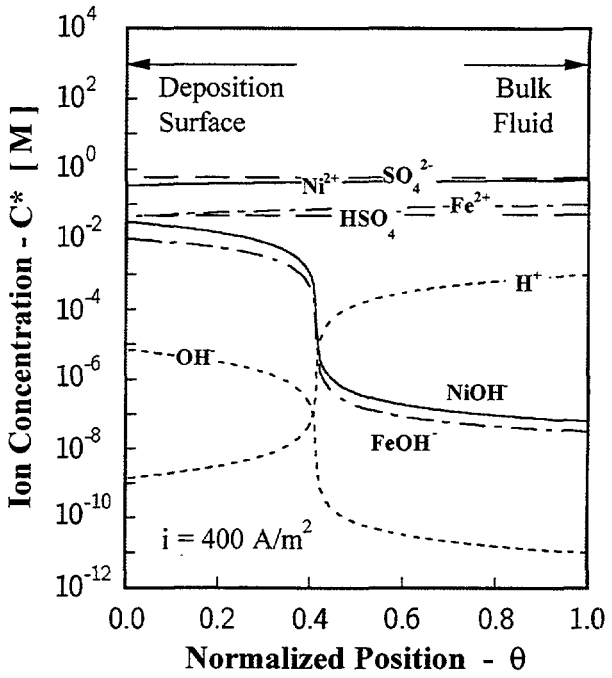

Figure 2. Distribution of ion species through a LIGA mold feature for codeposition of nickel and iron from a sulfate bath. Species concentrations change rapidly through the thickness due to an abrupt increase in pH. Note that total concentrations of the iron and nickel bearing species do not vary significantly from the mold top (right) to the deposition surface (left). Mold height is $h = 100$ μm and the imposed current is 400 A/m^2.

we conclude that ion drift is generally limited to less than about 10% of the diffusive flux for all problems of practical importance to LIGA. Their analysis similarly did not include either local or global electroneutrality. Instead, this condition was replaced by a requirement that the total concentration of sulfate species was uniform across the diffusion layer. Despite this discrepancy, the two results remain in good agreement, and this suggests that the solutions may also be insensitive to the use of either the Poisson equation or electroneutrality to determine the electric field. By solving the equations using both of these approaches, we have confirmed that this is again the case for problems of practical importance to electroplating for LIGA device fabrication. This is an important observation since the computational effort required for the two methods differs by several orders of magnitude; the Poisson equation is notoriously difficult to solve in the context of a transport problem owning to the extremely large value of the term $4\pi e/\epsilon \approx 10^{14}$ on the right of Eq. (4a).

Figure 3 shows sample calculations of the local pH for the same conditions used to produce Fig. 2, except that here the total current is varied between 100 and 400 A/m^2. The pH at the deposition surface is important in all plating processes since it affects the deposition morphology as well as the onset of hydrogen formation via hydrolysis. In Fig. 3 we see that the pH at the deposition surface (left of plot) remains nearly constant at the bath value up to a critical current density of about 100 A/m^2. The surface pH

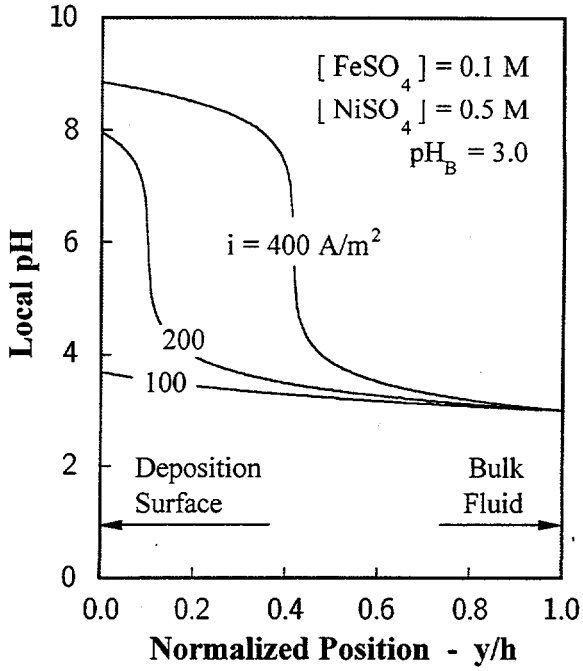

Figure 3. Local pH through mold thickness of a LIGA feature. The pH at the deposition surface (left) increases rapidly at current densities above 100 A/m^2. These currents are still well below the diffusion limited current of about 1100 A/m^2. High pH at deposition surface leads to poor metal morphology and hydrogen generation.

then abruptly climbs and the region of high pH moves off the surface toward the mold top as the current is further increased.

An important consequence of these results is that the currents shown in Fig. 3 are well below the diffusion limited current for this mold height. For a simple diffusion layer, this limiting current is given by

$$I_{\text{lim}} = 2F\frac{c_0 D}{h} \tag{20}$$

Based on a combined bath concentration of $c_0 = 0.6 \times 10^3$ mol/m^3, $D \approx 10^{-9}$ m^2/s and $h = 100$ μm, the limiting current is $I_{\text{lim}} = 1100$ A/m^2. Thus dramatic increases in the surface pH are evident when the imposed current is only about 20% of the limiting value.

Because pH at the deposition surface strongly affects the morphology of deposited metal, it provides one basis for selecting a desired current density. Since deposition rate is proportional to current (provided that current efficiencies remain near unity), the highest possible current is desired in order to minimize the total processing time. However, excessive current densities lead to poor morphology, so some optimum current must exist. To help identify these optimum currents for a sample problem, we have made a series of calculations for nickel deposition from a 1.0 M sulfate bath at an initial pH of three. In these calculations, the surface potential was adjusted to a point where the surface pH reached a specified value of either four or nine. The results of these calculations are shown in Fig. 4.

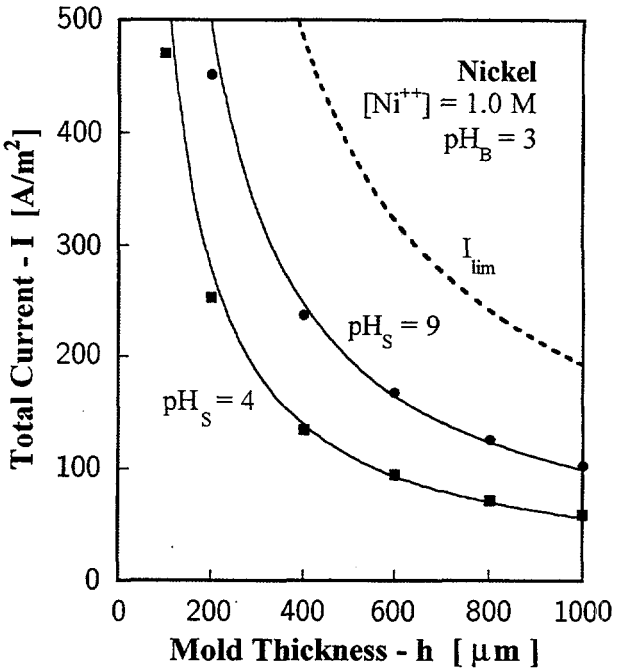

Figure 4. Allowable total currents as a function of mold thickness, h. Numerical solutions (symbols) were obtained for currents yielding a specific pH at the deposition surface by iteratively adjusting the surface potential. The dashed curve is the diffusion limited current given by Eq. (20). Solid curves are fixed fractions of 0.29 ($pH_S = 4$) and 0.52 ($pH_S = 9$) of the diffusion limited current.

The symbols shown in Fig. 4 are the computed total currents corresponding to a given pH at the deposition surface, for a given mold height, h. The dashed curve in this figure is the diffusion limited current given by Eq. (20). The two solid curves are simply the diffusion limited current shifted downward by a fixed multiplicative factor. Currents along the solid curve for $pH_S = 4$ are 29% of the limiting values, while those for $pH_S = 9$ are 52% of the limiting values. The generally good agreement between these solid curves and the numerical results over a wide range of mold thicknesses indicates that the transport problem scales well with mold thickness, and that a given increase in surface pH will correspond roughly to given ratio of the actual and limiting currents. These results can therefore be scaled approximately to other bath compositions simply by increasing or decreasing the currents shown in proportion to the actual bath ion concentration. Moreover, plating solutions other than nickel sulfate will probably exhibit similar behavior since the effective binary diffusivities of all small ions in an aqueous solution is order 10^{-9} m^2/s. Only the addition of pH buffers to the plating bath is likely to have a strong influence on this conclusion [20].

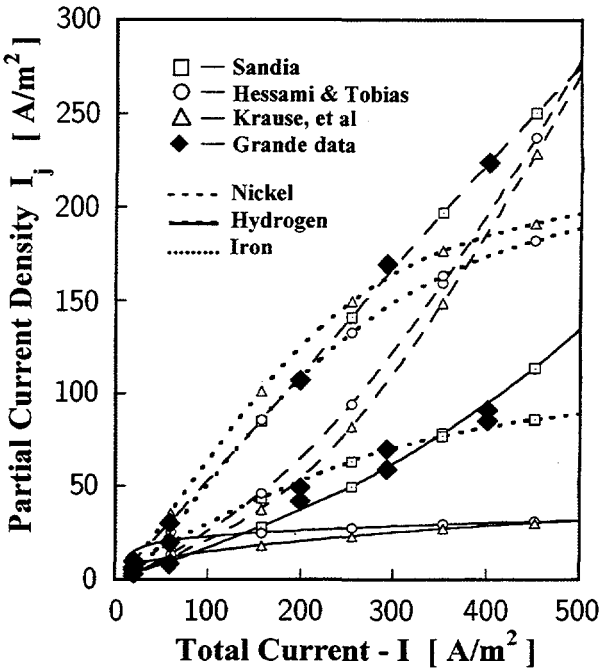

Figure 5. Partial iron, nickel and hydrogen currents for a 0.5 M $NiSO_4$ and 0.1 M $FeSO_4$ bath at a nominal pH of 3. Previous kinetics models (open symbols) do not agree well with measured results (closed symbols). Newly-developed model (open squares) closely match experimental results over a wide range of total current densities.

Electrode Kinetics

Although ion transport mechanisms and related material properties are fairly well understood, there is considerable uncertainty in defining the nature and kinetics of electrode reactions. In recent years Hessami and Tobias [17], Matlosz [21], and Krause, et. al. [18] have formulated alternative reaction mechanisms, including associated kinetics equations, intended to explain anomalous codeposition of nickel and iron. The anomaly in the process is that relatively much more iron is deposited than is explained by its ion concentration in the electrolyte [23,24]. Further, the composition of the deposit depends not only on the bath composition, but also very strongly on the total current. Each of these models is conceptually distinct, each is consistent with a limited subset of data, yet none can explain all observed results. As seen in Fig. 5, even the qualitative behavior of these three models is quite different when all three are applied to the same plating conditions. Although all three models indicate increasing dominance of iron at high current, the slopes and crossover points differ significantly among the models.

If the currents of Fig. 5 are instead plotted as a function of the electric potential, we find nearly an order of magnitude variation in deposition rates between these models and factor-of-two differences in their Tafel slopes for elemental deposition of nickel in the absence of iron. Moreover, the data of Grande and Talbot [25] indicates that nickel deposition increases in the presence of iron, whereas that of Dahms and Croll [26], used to produce their kinetics model, suggests just the opposite. We are currently

seeking to explain some of these apparent inconsistencies by a model that recognizes the dependence of deposition kinetics on the alloy composition of the plating surface.

This new model is based on the observation that reference potentials for the electrode kinetics are specific to deposition on a surface consisting of the metal of the ion being deposited. Since this is not the case for alloy deposition, the reference potentials must be adjusted to reflect the instantaneous composition of the deposition surface. The difficulty in implementing this model is that the surface composition depends on the iron and nickel currents, and these are the very quantities we are seeking to compute. To solve this problem we use an iterative method in which the reference potential for each species is shifted by an amount proportional to the partial current densities of all other species. From initial guesses of each partial current, shifts in all reference potentials are first computed. The partial and total currents are then calculated using the shifted reference potentials, and these currents are then used as new guesses for repeating the iteration. This method usually converges quickly, and the results provide much better agreement with measured currents and potentials over a wide range of conditions than do previous models.

Experimental Method

The objective of our experimental work was to observe the effects of mass transport limitations on electroplating under conditions similar to those found in LIGA applications. The apparatus was designed to establish a well-defined feature geometry and well-characterized fluid flow external to the mold, so that experimental results could be compared readily with those of our numerical models of the ion transport and deposition processes. The experimental system is intended to mimic the essential characteristics of electroplating for LIGA components, in particular, these investigations have focused on feature geometries having high aspect ratios. The observables in these experiments included current efficiency and cell voltages during electrodeposition, and the morphology of the deposits produced at various applied current densities.

The configuration of the electroplating apparatus is shown schematically in Fig. 6. The apparatus consists of a closed channel having a rectangular cross-section through which an electroplating solution can be pumped at various flowrates. The channel was machined from polycarbonate (Lexan) to allow visual observation during setup and operation. The channel is nominally 0.3 m long and the cross-section is 50 mm wide by 20 mm high. A cathode mold, containing several identical recessed electrodes whose recess diameter and length can be varied, and an anode, appropriate to the metal being deposited, are mounted in opposite walls of the flow channel with faces parallel to the direction of flow and flush with the surfaces of the wall. The reservoir of plating solution is maintained at its operating temperature by an immersion heater and is mechanically stirred to maintain uniform temperature and composition as the solution is recirculated. Isolation valves are incorporated into the flow loop to permit initial evacuation of the plating cell using a small mechanical vacuum pump, thereby ensuring that the cathode recesses will be completely filled with liquid when the plating solution is backfilled into the cell.

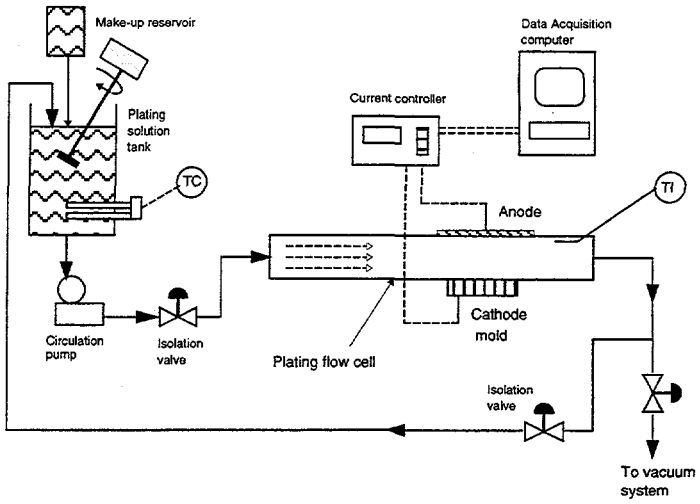

Figure 6. Schematic diagram of the flow cell electroplating apparatus.

A photograph of the cathode mold mounting arrangement on the plating cell is shown in Fig. 7. The cathode mold is clamped against the channel wall by the metal frame and screw to seal against leakage. The holes are typically oriented such that the cathode sheet faces upward to allow gas bubbles to rise away from the deposition surface. We used cylindrical cathode molds as such geometry is readily amenable to computational modeling. Cathode molds were machined from acrylic rod stock (Lucite) and typically had as many as eight identical cylindrical holes drilled completely through molds of various thicknesses. By varying the diameter, d, of the holes and the thickness of the mold, h, a wide range of aspect ratios, $A = h/d$, were produced by conventional machining methods. Although the absolute dimensions of these molds were much larger than typical LIGA masks that are produced lithographically, aspect ratios as large as 25 were achieved without the complexity and expense of using the synchrotron-based LIGA process.

Electroplating experiments were conducted using a commercial nickel sulfamate solution at a nominal temperature of 50 C. Electroplating was performed at constant current using a galvanostat-potentiostat (Model 363, Princeton Applied Research, Princeton, NJ) to control the applied current and to monitor the anode-to-cathode polarization during plating. A Macintosh SE computer operating OmegaBench data acquisition hardware and software (Omega Engineering, Stamford, CT) collected and stored the data (cell voltage, current, total charge) during each experiment. The current output of the data acquisition system agreed with a NIST-traceable ammeter within 0.5%. Current densities varying from 11 to 1300 A/m^2 were applied to a number of cathodes over periods as long as 24 hours to produce deposits having a thickness of about 1 mm. Annealed copper sheet, 75 μm thick, was used as the cathode in all experiments and was cleaned in hot caustic solution, pickled in hydrochloric acid, and rinsed, before being mounted on the cathode mold. The anode was a slug of high-purity nickel anode material that had been machined such that the upper surface could be sealed against the wall of the flow cell by a rubber O-ring. The active surface of the anode was a flat disc having a surface area of approximately 500 mm^2, much larger than that of the cathode

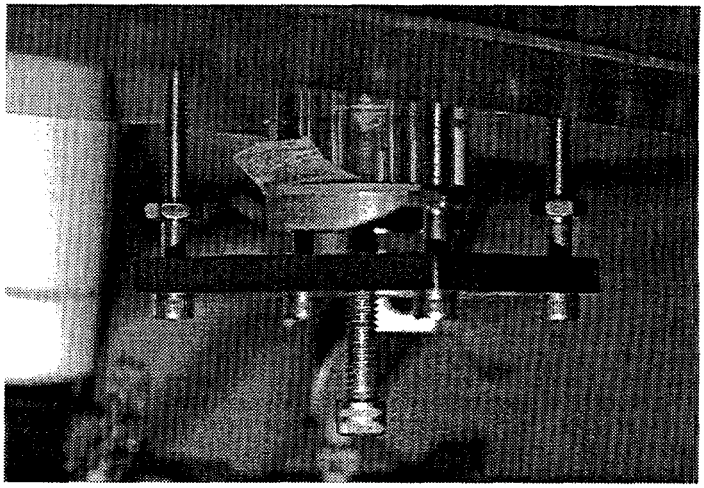

Figure 7. Close-up view of the flow cell apparatus showing the cathode mold assembled for an experiment. The tab protruding on the left of the cathode mold (clear cylinder) is the cathode sheet.

mold in any experiment. The anode disc and the patterned cathode were axially aligned to produce uniform polarization of the segments of the cathode mold during plating.

The cathode molds used for these experiments had cylindrical recesses ranging from 1.7 mm to 6.3 mm in diameter and depths ranging from 10 to 43 mm, producing aspect ratios between 1.6 and 25. A detail view of a typical cathode mold assembly is shown in Fig. 8. Eight symmetrically arranged holes are evident within the circle defined by the O-ring used to seal the mold against the wall of the channel. The right photo shows the typical appearance of the plated dot pattern produced on a copper cathode substrate. A close-up view of several holes in the cathode mold during the plating process is shown in Fig. 9. The disc of material indicated is the electrodeposit, as observed using a low-magnification stereomicroscope. Depending on the current density employed in an experiment, gas bubbles were often observed rising from or attached to the surface of the cathode.

The cathode sheets were weighed before and after plating to determine the mass of the electrodeposit and, given the total coulombs passed, the current efficiency. Electroplated deposits from several experiments were prepared metallographically to determine the uniformity of plating from cross-sectional views and etched to reveal the microstructure of selected deposits. The samples were etched using a mixture of glacial acetic acid, nitric acid and water (50:20:10, volume ratio). Samples were examined using optical and scanning electron microscopy.

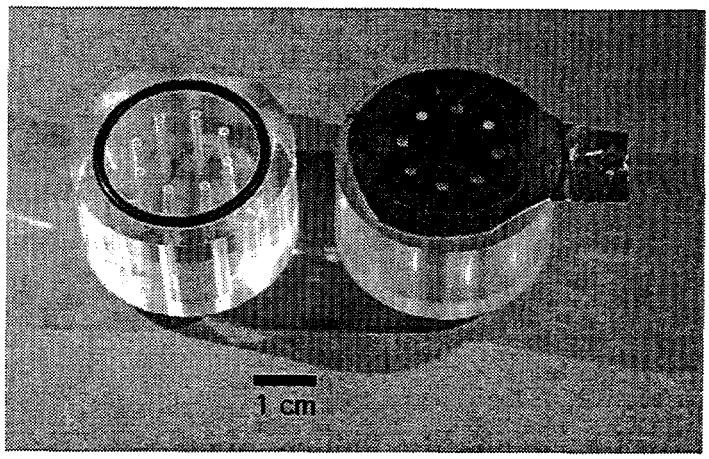

Figure 8. Photograph of a machined high aspect-ratio cathode mold (left) and a copper sheet that shows the resulting pattern of plated nickel columns.

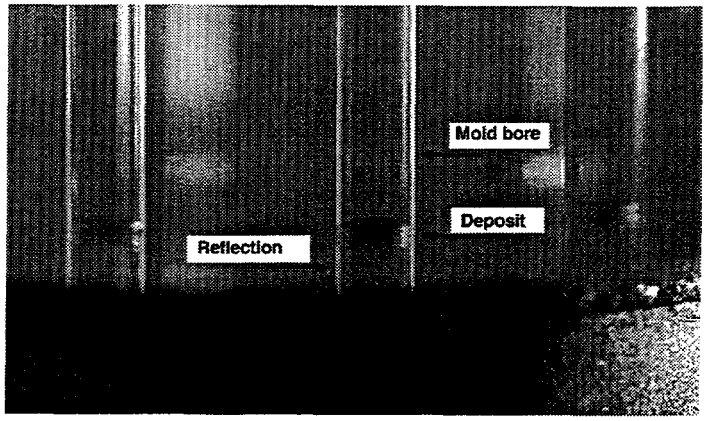

Figure 9. Close-up photograph of nickel deposits being plated in the bores of a recessed cathode mold. The diameter of the bore is 1.7 mm. The apparent continuation of the tube below the deposit is a reflection from the metal foil used as the substrate for plating.

Experimental Results

The macroscopic morphologies of the electroplated deposits clearly show that the uniformity of plating on recessed cathodes deteriorates significantly as the applied current density is increased above a threshold value specific to each mold geometry. An example of this behavior is shown in Fig. 10 where photographs taken using a 50X (nominal) stereo-microscope camera reveal the surface appearance of typical electroplated nickel columns. The aspect ratio of this mold was 25 and the current density increased from 108 to 646 A/m^2 as indicated in the caption. At current densities up to about 320 A/m^2, smooth, uniform deposits were obtained. Although a few small protrusions or cavities (due to bubbles persistently attached to the surface) are evident, the surfaces are generally flat. At current densities of about 400 A/m^2 or more, the uniformly flat surface was disrupted and nodular deposits formed. The formation of

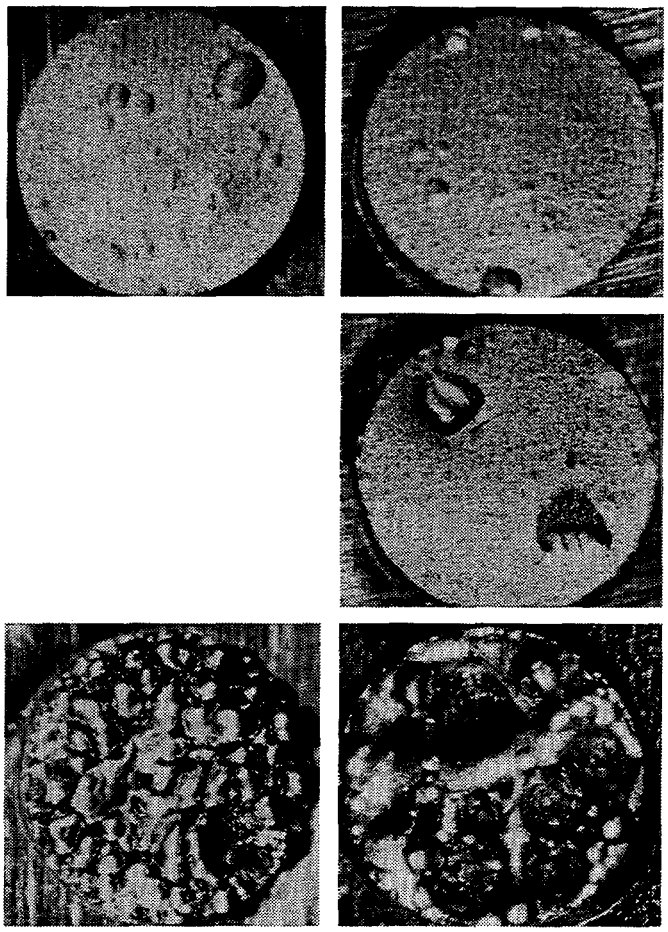

Figure 10. The effect of current density on the macroscopic morphology of nickel deposits on recessed cathodes for which d = 1.7 mm and aspect ratio was 25. Reading clockwise from top left, current densities are 108, 215, 323, 430, and 646 A/m^2. The images were obtained by optical microscopy.

bubbles was also aggravated, which resulted in porosity in the deposits. For comparison, note that nickel is typically plated in agitated tanks at current densities of 200 to 800 A/m^2, and that uniform deposits are produced under such conditions [27].

Despite the differing appearances of the deposits shown in Fig. 10, the current efficiency (C.E.) of the deposition process was quite high regardless of current density. Current efficiency was determined by weighing the cathode foil before and after plating and comparing the mass of the deposit to that calculated based on the Faradaic equivalent for the total charge passed during the experiment. These data are collected in Table 1 for tests in which the mold bore diameter varied from 1.7 to 6.3 mm. The latter diameter was chosen as it was the closest that the apparatus used here could approach plating on a surface for which the aspect ratio was zero, while keeping all other factors unchanged, due to the necessity of sealing the cathode mold. The data in the table indicates that C.E. was generally high. Those instances where C.E. exceeds 100% are

due to small amounts of foreign material trapped in the deposits, which usually had a net mass of only several to tens of milligrams.

In many experiments, and particularly those conducted at large current densities, gas bubbles were observed attached to the surface of the cathode. These bubbles obstructed the uniform deposition of nickel and significantly affected the macroscopic appearance of the deposits. While small (< 0.1 mm) bubbles were often seen detaching from the surface and rising upward through the bores, some bubbles remained attached throughout the plating experiments. In these cases, smooth curved surfaces were observed that replicated the shape of the attached bubble as the deposit grew around the obstruction. An example of such a cavity can be seen at the 11 o'clock position of the top row, right photograph in Fig. 10. In other instances, porosity was created within the deposit, perhaps as the deposit engulfed a bubble and developed nodules.

The bubbles are comprised of hydrogen that is formed by a secondary cathodic reaction that competes with the nickel reduction reaction. As the pH of the nickel sulfamate solution was nearly 4 in all of the tests, the reduction of water is likely more significant than the reduction of hydrogen ions to produce gaseous hydrogen. Note that the current efficiency obtained at unobstructed cathodes in agitated plating baths is typically 99% [28]. Although the current efficiency of nickel plating was ordinarily at least 98% in virtually all of these experiments, the remaining nominal 1% of the current is sufficient to create bubbles having the dimensions observed here. If the stagnant volume of plating solution in the mold bores cannot dissolve hydrogen as quickly as it forms at the surface of the growing deposit, bubbles will nucleate and grow. Often, such bubbles were seen to detach from the surface and rise through the bore. Despite the presence of surfactant in the plating solution, persistent attachment of bubbles was observed and such bubbles often could not be dislodged by mechanical impacts of the plating cell.

The most remarkable result of these experiments is that the measured plating currents are 4 to 137 times greater than the diffusion-limited current given by Eq. (20). This may be seen in Table 1 which includes a Sherwood number representing the ratio of measured current to diffusion-limited current. This dimensionless parameter is usually defined as the ratio of the actual mass transfer at a surface to that which would have occurred by diffusion alone. An analogous interpretation applies to electroplating currents, because charge transfer and mass transfer rates are linearly related through Faraday's constant and ion charge. As seen in Table 1, Sherwood numbers in excess of 40 were observed at the highest current density for all aspect ratios.

In search of an explanation for these surprising results, a number of hypotheses were assessed by scoping calculations. It was found that in some of the shorter runs, the initial inventory of metal ions stored within the recesses could account for a substantial fraction of the total amount deposited, but in most cases the plating time was long enough to exhaust that supply. Thus, it was necessary that metal ions be resupplied to the plating surface by a steady transport process. Additional calculations suggested that forced flow over the recesses could not produce significant convective mass transfer to the plating surface. However, it was estimated that depletion of metal ions at the bottom of the mold could produce a large enough reduction in fluid density to strongly

Cavity Diameter (mm)	Aspect Ratio	Current Density (asf)	Current Efficiency	Sherwood Number	Rayleigh Number
1.70	10	10	99.7	6.9	3.3×10^9
"	"	30	127.5	20.5	"
"	"	40	101.3	27.5	"
"	"	50	99.8	34.4	"
"	"	60	94.2	41.1	"
"	"	70	97.3	48.0	"
"	"	70	99.7	48.0	"
1.70	15	20	100.2	20.5	1.1×10^{10}
"	"	40	100.5	41.1	"
"	"	60	98.1	61.6	"
"	"	60	98.2	61.6	"
"	"	80	96.4	82.2	"
1.70	25	20	100.8	34.4	5.2×10^{10}
"	"	40	107.2	68.7	"
"	"	60	98.1	103.1	"
"	"	60	99.2	103.1	"
"	"	80	89.6	137.5	"
3.18	8	20	100.8	20.5	1.1×10^{10}
"	"	40	99.3	41.1	"
"	"	60	99.7	61.6	"
"	"	60	99.2	61.6	"
"	"	80	99.6	82.2	"
"	"	80	99.5	82.2	"
6.35	1.6	10	100.6	4.1	7.1×10^8
"	"	40	99.6	16.4	"
"	"	60	99.3	24.6	"
"	"	80	104.3	32.9	"
"	"	100	100.9	41.1	"

Table 1. Current efficiency of nickel plating in cylindrical recesses having various aspect ratios. Note that 1 A/ft^2 (asf) is about 10.8 A/m^2.

circulate the fluid. Rising hydrogen bubbles might also produce the same effect, though probably not in a steady and repeatable manner.

To verify that buoyancy-driven convection was responsible for the enhanced transport, we performed additional experiments in which the plating apparatus was turned upside down. In this inverted configuration, maximum plating currents were reduced by more than an order of magnitude, compared to those observed for an upward facing plating surface. Thus, there is strong evidence that buoyancy effects can increase plating rates by one or two orders of magnitude in high aspect ratio feature. Such large plating currents will be of great benefit in reducing LIGA plating times, provided that they can be reliably employed at scales much smaller than those used in our experiments. Those questions are being answered through modeling studies described in the next section.

Buoyancy-Driven Convection

Having experimentally discovered and confirmed the importance of buoyancy-driven convection in plating of high aspect features, our modeling effort turned toward improved understanding of this transport process. Since it is possible that formation and release of hydrogen gas bubbles played a significant role in the laboratory configuration, it is necessary to learn whether strong convection can be driven by ion depletion in the absence of bubbles. This distinction is critical because current densities must generally be held below the bubble formation threshold to assure acceptable deposit morphology. In contrast, a moderate level of ion depletion, say 50% at the plating surface, may greatly improve the transport of both metal ions and dissolved hydrogen without compromising deposit morphology. Aside from addressing this issue, modeling is also needed to extrapolate from the feature widths of 1.7 to 6.3 mm, used in our experiments, to LIGA feature widths of 10 microns or less. To meet these needs and to prepare for future process optimization, we developed and verified a two dimensional model of convection in high aspect features.

Buoyancy-driven fluid motions and related transport processes have been extensively studied, particularly in heat transfer applications where the fluid density varies with the temperature. Although such temperature variations may exist in electroplating processes, the corresponding density variations are no greater than 0.3%, even for a temperature difference as large as 30 C. Of far greater importance is the local reduction in fluid density resulting from the depletion of metal ions at the plating surface. Removal of these heavy ions from the adjacent electrolyte reduces the local fluid density by as much as 10% when plating at relatively high rates from 1 M nickel baths. Because of its reduced density, the depleted electrolyte rises from an upward facing electrode, permitting the inflow of fresh electrolyte.

Despite the relatively large density differences associated with ion depletion, there is very little mention of natural convection in the electroplating literature [29,30]. This is because natural convection plays only a secondary role in conventional plating of flat surfaces; there fresh electrolyte is supplied to the plating surface by vigorous stirring of the bath. Such forced flows of electrolyte may also help to stir the upper portion of a LIGA feature such as a narrow trench or a hole. However, the strength of the this

forced convective transport decreases logarithmically with the ratio of feature depth to width [31,32], making it nearly irrelevant for aspect ratios beyond three or four. Thus, only buoyancy-driven convection is important to electrodeposition in high aspect-ratio features.

Although the literature of heat and mass transfer includes hundreds of studies of natural convection, none deal directly with the configuration of interest here [33]. Studies addressing tall slender LIGA-like domains are mainly concerned with transport induced by horizontal gradients of temperature and density, as in the so called storm window problem. Conversely, previous studies exploring vertical density gradients have focused on relatively shallow layers, as in the classical Rayleigh-Benard problem that is posed on a heated plane of infinite width. There are, of course, numerical studies of natural convection in rectangular domains having vertical density gradients [34-37], but none exceeds an aspect ratio of two. Similarly, experimental studies are limited to a maximum aspect ratio of four, and there the Rayleigh and Reynolds numbers are orders of magnitude greater than those encountered in LIGA [38]. Thus, the regime of interest for LIGA remains unexplored.

To better understand the role of natural convection in electroplating of deep recesses, we have performed a series of numerical simulations. These calculations describe flow and transport in deep trenches like that shown in Fig. 1. The results, presented below, indicate that natural convection can easily provide an order of magnitude increase in ion transport, consistent with our earlier experimental observations. However, it is also found that convective flow instabilities may produce a variety of different flow patterns and transport rates, even under conditions of fixed geometry and nearly identical external constraints. Thus, a thorough understanding of the process will be needed to gain the benefits of enhanced transport in a predictable manner that aids, rather than hinders, uniformity of results.

Governing Equations: Buoyancy-Driven Transport

The equations describing steady-state conservation of mass for a nearly incompressible fluid containing multiple chemical species may be written

$$\nabla \cdot \mathbf{u} = 0 \tag{21}$$

$$\nabla \cdot (\mathbf{u}c) = \nabla \cdot (D \nabla c) \tag{22}$$

where $\mathbf{u} = u\mathbf{i} + v\mathbf{j}$ is the fluid velocity vector, c is the partial molar density of any chemical component, and D is the effective binary diffusivity for that species. Rather than solving continuity equations for all species of a complex bath, we now focus attention on a particular component that is largely responsible for density reduction at the plating surface. Thus, c will represent the concentration of a singular depositing metal ion.

Under the customary Boussinesq approximation, the fluid density is treated as though it were uniform except in evaluating the buoyancy force, $\rho\mathbf{g}$, appearing in the following statement of momentum conservation.

$$\rho(\nabla\times\mathbf{u})\times\mathbf{u} = -\nabla p - \rho\mathbf{g} + \nabla\cdot(\mu\nabla\cdot\mathbf{u}) \tag{23}$$

Here, p and μ are the pressure and the kinematic viscosity. The density variations that drive the motion can be related to ion concentrations by a linear approximation of the form

$$\rho = \rho_0 + \Delta\rho\left(\frac{c-c_0}{c_0}\right) \tag{24}$$

in which c_0 and ρ_0 are the bath concentration and density, and $\Delta\rho$ is the density reduction that results from full depletion of the plating species. To isolate the effects of buoyancy, the electric field forces have been omitted from the momentum balance. As shown earlier, the associated ion drift velocities provide only a modest enhancement to diffusive transport under typical plating conditions. For further simplicity, the viscosity and diffusivity will be presumed uniform and our example calculations will be restricted to some idealized, but fundamental, two dimensional geometries.

To facilitate numerical solution by finite difference methods, it is convenient to rewrite the governing equations for two dimensional flow in terms of the normalized stream function ψ^* and vorticity ω^* [39,40]. The stream function is defined in a manner that ensures satisfaction of the bulk continuity equation.

$$u^* = \frac{\partial\psi^*}{\partial y^*} \qquad \text{and} \qquad v^* = -\frac{\partial\psi^*}{\partial x^*} \tag{25}$$

Here, the position coordinates and velocity components are respectively scaled by the feature height, h, and a reference velocity, D/h.

$$x^* = \frac{x}{h}, \quad y^* = \frac{y}{h}, \quad u^* = \frac{uh}{D}, \quad v^* = \frac{vh}{D}, \quad \psi^* = \frac{\psi}{D}, \quad \omega^* = \frac{\omega h^2}{D} \tag{26}$$

In terms of these scaled variables and a normalized metal ion concentration, $c^* = c/c_0$, the species conservation equation becomes

$$u^*\frac{\partial c^*}{\partial x^*} + v^*\frac{\partial c^*}{\partial y^*} = \frac{\partial^2 c^*}{\partial x^{*2}} + \frac{\partial^2 c^*}{\partial y^{*2}} \tag{27}$$

Further, by cross differentiation and summation of the x and y components of the momentum equation, the pressure is eliminated from the following expression of momentum conservation

$$\frac{1}{\mathrm{Sc}}\left(u^*\frac{\partial\omega^*}{\partial x^*} + v^*\frac{\partial\omega^*}{\partial y^*}\right) = -\mathrm{Ra}\left(\frac{\partial c^*}{\partial x^*}\cos\phi + \frac{\partial c^*}{\partial y^*}\sin\phi\right) + \frac{\partial^2\omega^*}{\partial x^{*2}} + \frac{\partial^2\omega^*}{\partial y^{*2}} \tag{28}$$

in which the normalized vorticity is defined in terms of velocity gradients.

$$\omega^* = \frac{\partial v^*}{\partial x^*} - \frac{\partial u^*}{\partial y^*} \tag{29}$$

Note that the buoyancy forces driving convective motion now appear as spatial derivatives of the metal ion concentration, c^*, and that ϕ is the inclination angle of the y axis, measured from the vertical. Finally, the stream function and vorticity are related through the equation

$$\omega^* = -\left(\frac{\partial^2 \psi^*}{\partial x^{*2}} + \frac{\partial^2 \psi^*}{\partial y^{*2}}\right) \tag{30}$$

as readily verified by substituting Eqs. (25) into Eq. (29). This last elliptic equation will be used to calculate the stream function from candidate values of the vorticity.

The two parameters appearing in the momentum equation are the Rayleigh and Schmidt numbers; both are written below in terms of the dynamic viscosity $\nu = \mu/\rho_0$.

$$\mathrm{Ra} = \frac{\Delta\rho\, g h^3}{\rho_0\, D\nu} \qquad \text{and} \qquad \mathrm{Sc} = \frac{\nu}{D} \tag{31}$$

Since the Schmidt number is typically of the order 10^3 for small ions in an aqueous solution, the advective vorticity transport on the left side of Eq. (28) is generally negligible. In this asymptotic regime, there is essentially no dependence of the solutions on the Schmidt number. The only remaining parameter is the Rayleigh number, a measure of the strength of the buoyancy-driven motion. For LIGA features having depths, h, ranging from 0.1 to 1.0 mm, the Rayleigh number is on the order of 10^5 to 10^8. This estimate is based on a relative density difference of $\Delta\rho/\rho_0 = 0.1$, as appropriate for a 1 M nickel bath and full depletion of metal ions at the deposition surface. The actual value of the normalized surface concentration is, however, controlled by the boundary condition at the plating surface.

Numerical Approach

The preceding partial differential equations are solved numerically on the T-shaped domain shown in Fig. 1. The lower rectangular part of the domain represents a trench-like LIGA feature of height h and width w. Since the side walls of the trench are electrical insulators, plating occurs on the floor alone. The wider region above the trench represents a portion of either a plating bath or of a channel used to supply fresh electrolyte. Although this bath or channel is actually much larger than the trench, only a small portion need be included in the computational domain, provided that the boundary conditions are judiciously chosen. To reduce sensitivity of the solution to the vertical location of the upper boundary, the horizontal shear stress, τ^*, is prescribed there rather than the velocity, and the flow is permitted to pass vertically through this boundary. If the vertical velocity is downward, the normalized concentration is set to unity on the upper boundary, as appropriate for the inflow of fresh electrolyte.

Conversely, for an upward flow, the vertical concentration gradient is set to zero, letting the boundary value approach that of the exiting flow.

$$\frac{\partial^2 \psi^*}{\partial y^{*2}} = \frac{\partial u^*}{\partial y^*} = \frac{\tau h^2}{\mu D} = \tau^* \qquad \text{and} \qquad c^* = 1 \quad \text{or} \quad \frac{\partial c^*}{\partial y^*} = 0 \tag{32}$$

A positive shear stress, τ^*, drives a horizontal flow above the feature, with fluid entering the top portion of the T-shaped domain through its left boundary and leaving to the right. At the inflow boundary, it is required that the vertical velocity be zero and that the normalized ion concentration be unity.

$$\frac{\partial \psi^*}{\partial x^*} = 0 \qquad \text{and} \qquad c^* = 1 \tag{33}$$

Similarly, for a minimally restrictive outflow boundary,

$$\frac{\partial \psi^*}{\partial x^*} = 0 \qquad \text{and} \qquad \frac{\partial c^*}{\partial x^*} = 0 \tag{34}$$

All of the impermeable solid boundaries, both within the feature and external to it, may be viewed as one continuous streamline on which

$$\psi^* = 0 \qquad \text{and} \qquad \frac{\partial c^*}{\partial \eta^*} = 0 \tag{35}$$

where η^* is in a direction normal to each surface. The first of these applies at all solid boundaries, while the second applies everywhere except on the deposition surface at the mold bottom. In addition, both of the velocity components are zero on all solid surfaces, and these conditions are reflected in the boundary values of vorticity that are calculated from the defining equation (29).

Although the plating surface is actually a moving boundary, its velocity is far too small to influence the flow and concentration fields. The ion flux to the plating surface is, however, of critical importance because it produces the density gradients that drive the flow. Rather than incorporating any specific electrode kinetics, we chose to apply a more generic boundary condition relating the incoming diffusion flux to a surface deposition rate that is proportional to the local ion concentration.

$$\frac{\partial c^*}{\partial y^*} = K^* c^* \qquad \text{on} \qquad y^* = 0 \tag{36}$$

To explore transport limitations, our sample calculations will employ a very large value of the dimensionless rate coefficient, K*, corresponding to a high current density and a small surface concentration.

The equations are solved numerically on a square mesh having 41 nodal points across the trench. Derivative operators are replaced by finite difference approximations to obtain a system of algebraic equations for the nodal point values of all dependent variables. The iterative solution procedure includes several steps: (1) solve Eq. (27) for

c^*_{ij}; (2) use derivatives of the new concentration field in solving Eq. (28) for ω^*_{ij}; (3) use the new vorticity field in solving Eq. (30) for ψ^*_{ij}; (4) differentiate the new stream function to calculate velocity components from Eq. (25); (5) differentiate the velocity field to calculate boundary values of vorticity from equation (29); and (6) repeat to convergence. Because of the strong coupling among all of the equations, there is little to be gained by matrix inversion of to obtain tentative solutions. Instead, each of the individual nodal equations are solved in sequence for the pivotal value that satisfies that equation with all other dependent variables held fixed at their most recent values. Only one iteration is performed for each field before proceeding to the next dependent variable in the sequence listed above. Convergence is generally improved by weighted averaging of new and old iterates.

Sample Calculations

The following results illustrate both the importance and the complexity of convective transport in electroplating deep features of high aspect ratio. As a prelude to buoyancy-driven flows, solutions are first presented for convection driven by external flow across the top of a deep feature. Subsequent sample calculations explore the combined effects of external flow and buoyancy. We will show that buoyant transport is clearly dominant in high aspect-ratio features, but that fluid speeds and transport rates may vary by a factor of two or more between equally likely flow patterns.

Figure 11 shows the calculated streamlines and concentration field for a flow driven by an external shear stress of $\tau^*=10^4$, a Rayleigh number of zero, and an aspect ratio of $A = h/w = 4$. This normalized shear stress is roughly that produced at the top of a 1 mm deep LIGA feature by a fluid speed of 60 mm/s in a channel of height 20 mm, like that used in the laboratory experiments described earlier. Since the general problem of a shear-driven cavity has been studied previously [32,34-37], this example serves both to validate our numerical procedure and to illustrate shear driven flow in the absence of buoyancy. We see that the streamlines of the external flow bend slightly downward into the cavity, increasing the local shear stresses at the upper edges of the cavity. This is one of the reasons for applying the external boundary conditions well above the mold top, since the velocity, shear stress and species concentration at the top of the feature are not known beforehand.

The shear-driven circulation within the trench of Fig. 11 consists of three counter-rotating cells, each having an aspect ratio of roughly 1.3. A preferred cell aspect ratio of this value, or perhaps slightly greater, is consistently observed for shear driven flows in all deep trenches, though deviations must obviously occur for noninteger ratios of trench depth to preferred cell size. The stream line pattern within each cell is nearly identical, so long as the Reynolds number, $\mathrm{Re} = uw/\nu$ is no greater than a few hundred. That criterion is well satisfied here since $\mathrm{Re} = \tau^*/\mathrm{S}A^2 < 1$. Despite this similarity of flow pattern, the maximum fluid speeds within each circulation cell decreases by a factor of roughly 10^3 from one cell to the adjacent cell below. The resulting six order-of-magnitude decrease in speed between the top and bottom cells of Fig. 11 motivated our

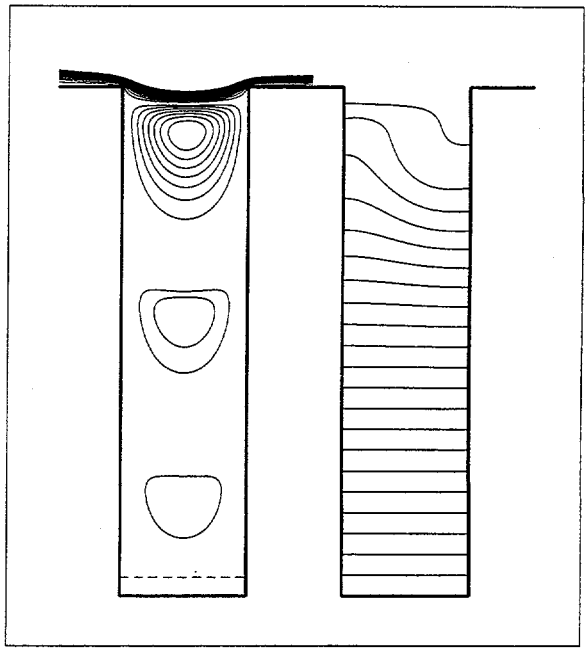

Figure 11. Stream lines and concentration isopleths for forced convection driven by horizontal flow above feature. Fluid speed within convective cells decreases by a factor of 10^3 from one cell to the next. Uniformly spaced horizontal isopleths indicate a condition of purely diffusive transport beneath the uppermost cell.

use of a logarithmic spacing between ψ^* values on the streamlines shown. Even then, the spacing is sparse in the lower cells.

A contour plot of the ion concentration field is shown on the right side of Fig. 11. The partial molar density, c^*, of any plating species is constant on each of the isopleths. In contrast to the logarithmic spacing of streamlines, the isopleths are separated by uniform increments of concentration. Thus, the equal physical spacing of isopleths along most of the trench indicates that the concentration gradient is uniform, as required for steady state transport by diffusion alone. Wider spacing of the uppermost isopleths is indicative of strong convective transport in the upper circulation cell. Note that the isopleths bend downward on the right side of the trench in response to the downflow of fresh electrolyte.

The Sherwood number, Sh, a figure of merit for convective transport, is the ratio of the total vertical transport by convection and diffusion to that which would occur by diffusion alone. Continuity requires that the Sherwood number for a steady process must be the same at all elevations in the feature. It is most conveniently evaluated at the plating surface where the vertical velocity must vanish and local transport occurs only by diffusion, whereupon

$$\mathrm{Sh} = \left(\frac{h}{D\Delta C}\right)\frac{1}{w}\int_0^w D\frac{\partial C}{\partial y}dx = A\int_0^{1/A}\frac{\partial c^*}{\partial y^*}dx^* \qquad \text{on} \qquad y^* = 0 \tag{37}$$

Applying this definition to the calculation of Fig. 11 yields a Sherwood number of 1.2, indicating only a 20% improvement over diffusion.

The fundamental limitation of forced convection transport in high aspect-ratio features is well illustrated by the example of Fig. 11. Even if the uppermost convective cell were perfectly mixed with a uniform concentration of $c^*=1$, the overall flux would still be limited by diffusion through the relatively stagnant lower region. The net effect of a strongly convective upper cell is a reduction in diffusion distance by a ratio of three to two, yielding a maximum Sherwood number of about 1.5. Further increases in the Sherwood number can only be obtained by convective transport in the second cell from the top. Since it rotates a thousand times slower than the cell above, a thousand-fold increase in the external shear force is needed to achieve significant convection in that cell and thereby increase the Sherwood number to a maximum of three. By this same reasoning, the external shear velocity would have to be increased by a factor of 10^{15} to obtain Sherwood numbers greater than two for an aspect ratio of ten.

Unlike external shear forces, buoyancy forces may induce strong vertical motions that are nearly independent of elevation. Such a flow field is illustrated in Fig. 12 for $\mathrm{Ra} = 10^6$ and, as before, $\tau^* = 10^4$. In contrast to a shear driven flow, only one elongated circulation cell is produced, rather than many cells of nearly unit aspect ratio. The relatively dense external flow now turns downward into the trench, then descends to the bottom where it loses some of its metal ions by diffusion to the plating surface. The depleted fluid then rises to the surface where it rejoins the external stream. The calculated circulation is counter clockwise, though a strong enough external shear would close the top of the cell and reverse its direction. Note that the streamlines of Fig. 12 are spaced uniformly in ψ^*, such that the volumetric flow rate between any adjacent streamlines is the same. Thus, the relatively uniform physical spacing of streamlines indicates that flow speeds are everywhere comparable, even in the turning region near the bottom.

The isopleths of Fig. 12 reveal a narrow boundary layer just above the plating surface. In this region the fluid motion is essentially horizontal, requiring that the vertical flux be carried by diffusion alone. The local vertical gradient must thus be steeper here than in the upper region where the flux is carried advectively by opposing vertical streams having differing ion concentrations. These side-to-side differences in concentration are apparent in the nearly vertical, rather than horizontal, orientation of the isopleths at midheight. As the descending fluid approaches the plating surface, it compresses the isopleths on the left side, whereas the ascending fluid expands the isopleths on the right. This asymmetry of motion results in the asymmetric flux profile indicated by a dashed curve in the left frame of Fig. 12. The peak flux occurs near the center, where the horizontal velocity is greatest and the diffusion layer is thinnest. The vertical scale of this flux profile is the same as in the preceding Fig. 11, so the magnitude is clearly greater in the present buoyancy-driven flow.

The ion flux to plating surface of Fig. 12 corresponds to a Sherwood number of about 14, exceeding that for the shear driven flow by more than a factor of ten. This level of enhancement is consistent with the concentration field, since the steep gradients are now confined to just 10% of the feature depth. Ion concentrations just above that layer are nearly equal to the bath concentration, shortening the diffusion distance by a factor of ten.

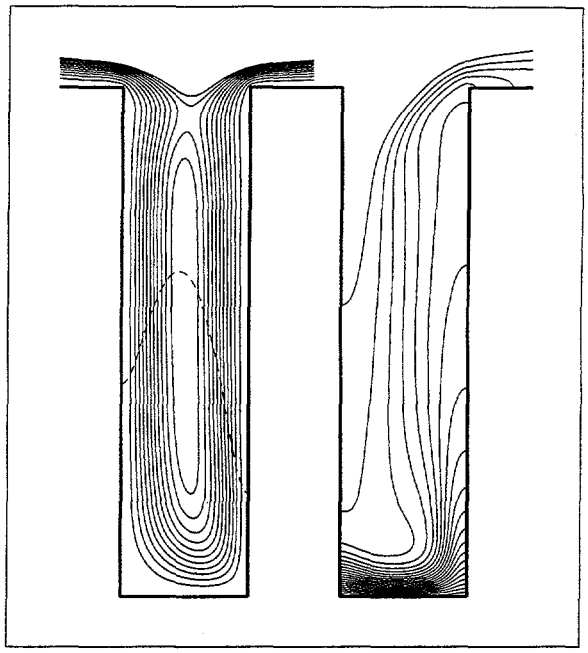

Figure 12. Stream lines and concentration isopleths for a buoyancy-driven flow with a Rayleigh number of 10^6. Strong convective motion carries fresh electrolyte deep into feature, reducing the thickness of the diffusive boundary layer at the plating surface.

Cell structures in buoyancy-driven flows may be altered significantly by slight variations in boundary or initial conditions. For example, the bicellular pattern shown in Fig. 13 has the same Rayleigh number and the same external shear stress as the monocellular pattern of Fig. 12. In fact, the bicellular structure is the preferred steady state solution. The single cell shown earlier was obtained by tilting the axis of the feature slightly off of vertical. In that tilted orientation, the component of gravity acting across the feature pulls the heavier fluid toward the lower sidewall. Thus, the tilt disfavors a bicellular pattern in which the opposite rotation of the cells necessarily places the heavier fluid on opposite walls in the upper and lower cells. Similarly, the direction and strength of the external flow or a slight bias of initial conditions can produce alternative flow patterns having factor of two differences in transport.

Multicellular flows are generally less efficient than single cell structures in transporting ion species. In the preceding examples, the Sherwood number decreased by almost a factor of three, from 14 to 5, between the single and multiple cells driven by nearly identical shear and buoyancy forces. The primary reason for this is apparent in the ion concentration fields of Figs. 12 and 13. Although both configurations have boundary layers at the deposition surface, only the bicellular flow has an additional diffusion layer at midheight. Here, steep concentration gradients are needed for diffusion exchange of ionic species between the upper and lower cells. Advection cannot enhance this exchange since no flow crosses between the two cells. The presence of two diffusion layers, rather than one, reduces the Sherwood number by roughly a factor of two. In addition, the presence of multiple cells generally reduces horizontal density differences, as also apparent in comparing isopleths, leading to slower fluid speeds and weaker transport.

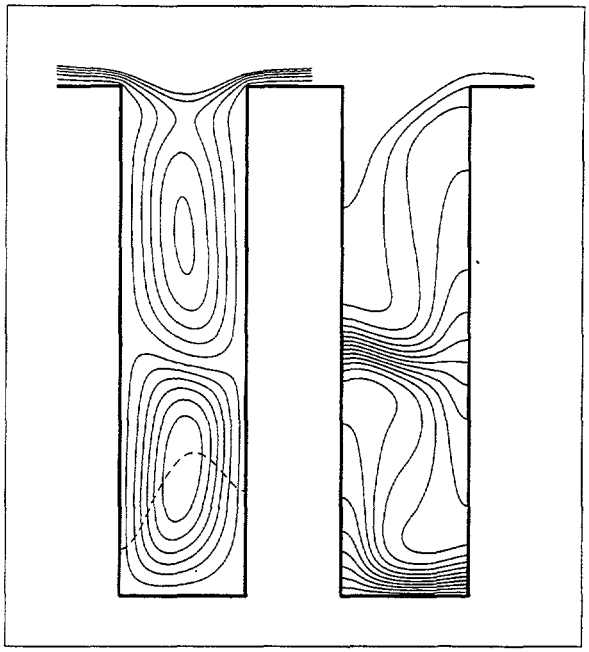

Figure 13. Bicellular convective motion for a Rayleigh number of 10^6. Although this flow pattern is more stable than a single cell, the transport is inhibited by the presence of a diffusion layer at midheight where ion species are exchanged between the two counter-rotating cells.

Contrary to intuition, an increase in the external fluid speed above the mold can sometimes reduce the overall transport to the plating surface. If, for example, the external shear is increased sufficiently in the bicellular flow of Fig. 13, the external stream will flow across the top of the mold, rather than circulating into the feature. The upper convective cell then becomes a closed loop that rotates faster than before, though in the opposite direction. The lower cell also reverses direction but increases in speed. However, despite these increases in fluid speed, the overall transport is reduced because a new diffusion layer must form at the top of the mold to transfer ions from the external flow into the top cell.

Increases in Rayleigh number generally produce stronger flows with increased transport. However, the diversity and complexity of flow patterns also increases with Rayleigh number. In addition, buoyancy-driven flows become less stable at high Rayleigh number and are likely to wander between two or more alternative patterns [33,41]. These observations are illustrated by the flow field shown in Fig. 14. Here, the Rayleigh number is 10^7, ten time greater than in previous calculations; the shear stress above the feature is the same as before. The time-averaged Sherwood number is 17, though instantaneous values range from 10 to 24.

The flow field shown in Fig. 14 consists of three closed cells, two of them side by side. In other instantaneous flow patterns these side-by-side cells are sometimes nearly symmetric about the vertical centerline of the feature and occasionally extend over most of the height. At other times one cell will dominate as the other shrinks into a corner. Occasionally, one of the lower cells becomes pinched at the waist and splits vertically in half, a process underway in the pattern displayed. In response to these gyrations, the

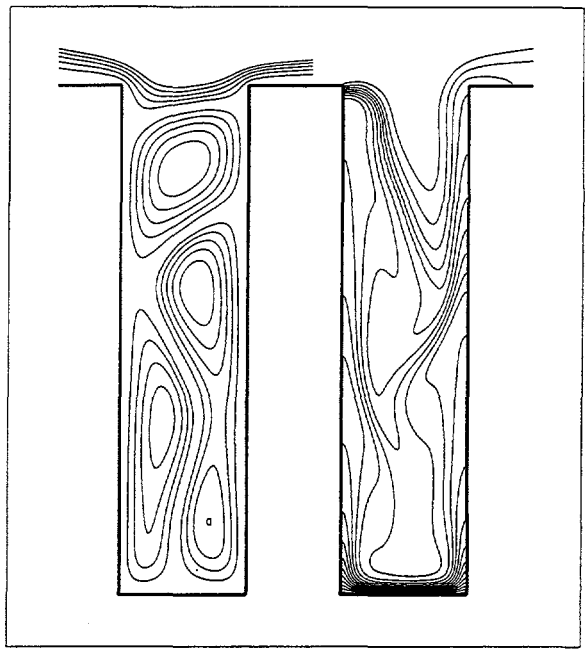

Figure 14. Pathological structure of flow for a Rayleigh number of 10^7. Flow is not truly steady, but instead oscillates periodically among several multicellular patterns. In response, instantaneous Sherwood numbers vary by about a factor of two.

upper cell expands and contracts in vertical extent. Despite all of this chaotic motion, the time average of the Sherwood number converges to a relatively stable mean on time scales much shorter than LIGA plating times. Thus, the chaotic nature of the flows may not be detrimental.

Three diffusive boundary layers are seen in the concentration field of Fig. 14. The steepest gradients and largest difference in concentration occur at the bottom. The other two boundary layers transfer ion species between the individual flow cells. Despite the relatively uniform appearance of the lower boundary layer, the flux at the center line is more that twice as great as the flux to the corners. The resulting excess metal deposition at the center should produce an arched lower boundary protruding into the mold that could either aggravate or help alleviate the nonuniformity of the flux. This question will be addressed in future calculations that evolve the shape of the deposition boundary.

The results of these numerical studies, are being used to guide the development of an analytical model that yields the Sherwood number as a function of the Rayleigh number, Schmidt number, and aspect ratio. The analytical model includes four basic features: (1) a momentum equation relating flow speeds to the horizontal difference in density between ascending and descending streams; (2) a horizontal density difference controlled by diffusion between these counter-flowing streams; (3) a boundary layer relationship between fluid speed and diffusion layer thickness; and (4) matching conditions between the vertical convective fluxes and the diffusion fluxes through boundary layers. An obvious difficulty in this endeavor is predicting the number of cells. However, at least for moderate Rayleigh numbers, the desired structure is a single cell which may be obtainable in practice by tilting the mold. It may even be possible to deduce the

number of cells though application of a stability criterion. At present, we simply treat the number of cells as an input parameter.

Rather than describing details of the analytical model, we briefly explain two of the most important results. Both of these analytical results are consistent with numerical calculations performed thus far but still require further verification. First, the analytical model predicts that no motion will occur for Rayleigh numbers less than a critical value that is strongly dependent on the aspect ratio, $A = h/w$.

$$\mathrm{Ra}_{\mathrm{crit}} = 192\, A^4 \tag{38}$$

For plating of metal ions from 1 M nickel baths into molds having a depth of 1 mm, this criterion suggests that significant convection will only occur for aspect ratios less than about 10 or 20. The allowable aspect ratio is twice as great in features half as deep. However, it is important to note that this criterion, and all of the foregoing calculations, address fluid motions that are two dimensional in a plane across the trench. If instead the fluid circulates in the long direction of a trench, the critical Rayleigh number is given by

$$\mathrm{Ra}_{\mathrm{crit}} = 192\, A^2 \left(\frac{h}{L}\right)^2 \tag{39}$$

in which L is the trench length. This would permit convection for aspect ratios as large as a few hundred in trenches having a length-to-depth ratio near unity. The more restrictive criterion would still apply to holes and short trenches. Thus, the varying geometry of individual features in a given mold may cause order of magnitude differences in deposition rates, and in many cases deposition rates will be subject to the diffusion limitations previously described.

A second result of the analytical modeling is that, for large enough Rayleigh numbers, the Sherwood number increases as the third root of Rayleigh number.

$$\mathrm{Sh} = 0.07\, \frac{\mathrm{Ra}^{1/3}}{N_{\mathrm{cell}}} \qquad \text{or} \qquad q = 0.07\, \frac{D}{N_{\mathrm{cell}}} \left(\frac{\Delta\rho\, g}{\rho_0 D \nu}\right)^{1/3} \tag{40}$$

Here, N_{cell} is the number of convective boundary layers and q is the ion flux to the deposition surface. This analytical result is in good agreement with those of previous experimental studies [38,42]. Also, since h disappears from the second of these equations, it follows that q is independent of the feature depth in a regime where this third root scaling holds. Under these circumstances, features of all depths and widths will plate at the same rate, a condition of great benefit to LIGA. Work is now in progress to verify this expectation and to further explore its application to LIGA plating.

Summary

In this study we have undertaken a combined theoretical and experimental program intended to help understand ion transport limitations and the effects of these limitations on electrodeposition for LIGA microdevice fabrication. Two numerical models have been developed: one describes either quasi-steady or transient one-dimensional diffusive transport of multiple ion species; the second describes two-dimensional diffusive and advective transport of a single species.

The first numerical model is implemented within a numerical framework that is readily adapted to a range of bath compositions, dissociation reactions, and electrode kinetics. To date we have focused on an eight-species model describing the simultaneous deposition of nickel and iron from a plating bath containing sulfuric acid and sulfates of both nickel and iron. The eight species presently included in the model are Fe^{2+}, $FeOH^{+}$, Ni^{2+}, $NiOH^{+}$, HSO_4^{-}, SO_4^{2-}, OH^{-}, and H^{+}. In this model, transport of these ion species to the mold bottom is governed by diffusion, electromigration, and the homogeneous reactions between species as they move toward the deposition surface. The model can be used to describe the deposition of either nickel or iron, as well as the codeposition of both species to produce various permalloy compositions. In addition to ion transport, the mathematical model describes the quasi-steady electric field within the mold and local deposition at the mold bottom.

Electric potentials are computed either by solving the Poisson equation relating the potential to the local charge density or by imposing a condition of local electroneutrality. The latter approximation provides solutions that are in good agreement with those using the more rigorous Poisson approach over a wide range of mold thicknesses and total current densities at a greatly reduced computational expense.

The Arrhenius kinetics of the electrode reactions are incorporated through Butler-Volmer equations relating the ion current density (equivalent to the deposition rate) to the electrode overpotential, temperature, charge transfer coefficient and reaction pre-exponential constants for each ion species. These equations are strongly coupled to the transport equations because electrode reaction rates depend strongly on local ion concentrations at the electrode surface. As part of this work we have developed a new kinetics model for the codeposition of nickel-iron alloys based on a reference potential for each ion species that varies with composition of the alloy surface. This new approach accurately describes the so-called anomalous codeposition of nickel-iron alloys (as measured by others) in which the alloy composition depends not only on bath composition but also on the total current.

The coupled species transport and electric field equations are solved using a coupled stiff differential and algebraic solver. Two main methods of solution have been developed. The first is a shooting technique in which governing equations are integrated in space from the mold top to the mold bottom, and the surface potential and partial iron and nickel currents are varied to satisfy Butler-Volmer relations at the deposition surface. This method is useful for obtaining very accurate solutions, but is limited to quasi-steady problems. The second method relies on a more conventional numerical approach in which the governing equations are spatially discretized and then integrated

in time. Although less accurate, this method is useful in solving the transient problems associated with pulsed plating techniques.

Our experiments were intended to explore essential features of LIGA-like metal deposition under well characterized conditions suitable for comparison with theoretical calculations. The apparatus consists of a transparent channel about 0.3 m long having a 20 by 50 mm rectangular cross-section. Electroplating solution was pumped from a temperature-controlled reservoir through this channel at a prescribed flow rate. A recessed cathode, analogous to a LIGA mold, and an anode, appropriate to the metal being deposited, are mounted in opposite walls of the channel with faces parallel to the flow and flush with the internal surfaces. A typical cathode mold consisted of a PMMA disc having several identical drill-holes in which metal was deposited. By varying the hole diameter and mold thickness, a range of aspect ratios from 1.6 to 25 were obtained.

Experiments were conducted using a commercial 1.36 M (80 g/ℓ) nickel sulfamate plating solution at a nominal temperature of 38 C. Current densities varying from about 100 to 1000 A/m^2 were applied to a number of molds over periods of approximately 24 hours. We found that surface morphology degraded significantly at the higher currents, and that larger aspect ratios produced poorer morphologies for a given current density. At an aspect ratio of 25, smooth uniform deposits were produced at currents up to about 300 A/m^2, but severe surface defects were observed at current densities of 400 A/m^2 and above. Current efficiencies were generally high for all of the test conditions, and efficiencies fell below 90% only at the highest current densities and feature aspect ratios.

The results of these experiments indicate that current densities well in excess of the diffusion limited currents may still yield acceptable morphologies in the deposited metal. This surprising result led to developing a second numerical model describing two dimensional convective motions within a single trench-like LIGA feature. The governing Navier Stokes equations include buoyancy forces resulting from ion depletion, as well as pressure, viscous and inertial forces. Although multiple species can be easily added, the current model includes only one transport equation describing diffusion and advection of a single metal ion. Rather than solving the primitive equations, the continuity and momentum equations are rewritten in terms of the stream function and vorticity and then discretized and solved on a rectangular finite-difference mesh. Fluid motions within the feature are driven both by external flow over the mold top and by depletion of metal ions at the deposition surface. The model was used to perform a series of numerical simulations over a range of external fluid speeds and fluid density variations typical of LIGA applications.

The results of these two-dimensional calculations first revealed that the experimentally observed hundred-fold increase in limiting currents cannot be attributed to fluid motion within the feature driven by external flow over the mold. Such flows produce a vertical stack of convective cells having nearly unit aspect ratio. However, the maximum fluid speed in each successive cell falls by nearly three orders of magnitude, so fluid motion more than a few feature widths from the mold top is negligible for any practical fluid velocity outside the mold. Conversely, buoyancy-driven flows were found to have elongated convective cells with vertical speeds nearly independent of elevation within the feature. Such flows can easily account for the hundred-fold increase in limiting current observed in our experiments. Even at the smaller scale of LIGA features,

transport rates and maximum current densities should exceed diffusion limits by more than an order of magnitude. Moreover, for sufficiently strong convection, plating rates should be independent of feature width and depth, a condition of great practical benefit to electroforming in the LIGA process.

Nomenclature

a_i electrode kinetics pre-exponential constant
c_i species concentration
D_i effective binary diffusivity
e elementary charge (1.602×10^{-19} C)
$\mathbf{E}$ electric field
F Faraday constant (9.648×10^4 C/mol)
h mold thickness
k Boltzmann constant (1.381×10^{-23})
m number of spatial grid points
n number of species
N Avogadro number (6.023×10^{23})
R ideal gas constant
S_i homogeneous reaction source or sink
T temperature
$\mathbf{u}$ fluid velocity
u horizontal fluid speed
v vertical fluid speed
V electric potential
w feature width
x transverse position
y vertical position
α_i charge separation constant
ϵ permittivity of vacuum (8.854×10^{-12} F/m)
ϕ normalized concentration
ψ stream function
ζ vorticity

Subscripts and Superscripts
0 denotes reference value
B of plating bath
S at deposition surface
* asterisk denotes normalized variable

Acknowledgment

This work was funded in part by a Sandia Phenomenological Modeling and Engineering Simulations LDRD, in part by a Materials Science and Technology LDRD, and in part by the Sandia Materials Science Research Foundation. Sandia is a multiprogram laboratory operated by Sandia Corporation, a Lockheed Martin Company, for the United States Department of Energy under contract DE-AC04-94AL85000.

References

1. W. Ehrfeld and L. Lehr, "Deep X-Ray Lithographie for the Production of Three-Dimensional Microstructures from Metals, Polymers and Ceramics," Radiation Physics and Chemistry, **45** (3), 349-365, 1995.
2. A. Maner, S. Harsch and W. Ehrfeld, "Mass Production of Microdevices with Extreme Aspect Ratios by Electroforming," Plating and Surface Finishing, 60-65, March 1988.
3. A. Rogner, J. Eichert, D. Munchmeyer, R. P. Peters, and J. Mohr,"The LIGA Technique–What Are the New Opportunities" J. Micromech. Microeng., **2**, 133-140, 1992.
4. W. Ehrfeld and D. Munchmeyer, "Three-Dimensional Fabrication Using Synchrotron Radiation," Nuclear Instruments and Methods in Physics Research, **A303**, 523-531, 1991.
5. H. Guckel, "Deep X-Ray Lithographie for Micromechanics via Synchrotron Radiation," Nuclear Instruments & Methods in Physics Research, **79** (1-4), 247-248, 1993.
6. C. K. Malek, K. Jackson, R. A. Brennen, M. H. Hecht, W. D. Bonivert and J. M. Hruby, "Deep Etch X-Ray Lithography at the Advanced Light Source: First Results," EIPB '94, Proceeding of the 38th Int. Symp. on Electron, Ion and Proton Beams, New Orleans, LA, May 31-June 3, 1994.
7. W. K. Schomburg, J. Vollmer, B. Bustgens, J. Fahrenberg, H. Hein, and W. Menz, "Microfluidic Components in the LIGA Technique," J. Micromech. Microeng., **4**, 186-191, 1994.
8. H. Lehr, W. Ehrfeld, B. Hagemann, K. P. Kamper, F. Michel, C. Shultz and C. Thurigen, "Development of Micromotors and Millimotors', Minimally Invasive Therapy & Allied Technologies, **6** (3), 191-194, 1997.
9. U. Wallrabe, P. Bley, B. Krevet, W. Menz, and J. Mohr, "Design Rules and Test of Electrostatic Micromotors Made by the LIGA Process," J. Micromech. Microeng., 4, 40-45, 1994.
10. K. H. Brenner, M. Kufner, S. Kufner, J. Moisel, A. Muller, S. Sinzinger, M. Testorf, J. Gottert and J. Mohr, "Applications of 3-Dimensional Micro-Optical Components Formed by Lithography, Electroforming and Plastic Molding," Applied Optics, **32** (32), 6464-6469, 1993.
11. B. Narasimhan and N. A. Peppas, "The Physics of Polymer Dissolution: Modeling Approaches and Experimental Behavior," Advances in Polymer Sciences, **128**, 157-207, 1997.

12. E. M. Lehocky, J. D. Wice, and I. Reid, "Dissolution Characteristics of Poly(methyl methacrylate) as an X-Ray Resist," Can. J. Physics, **65**, 975-978, 1987.
13. Y.Fukunaka, H. Doi, and Y. Kondo, "Structural Variation of Electrodeposited Copper Film with the Addition of an Excess Amount of H2SO4," J. Electrochem. Soc., **137** (1), 88-93, 1990.
14. D. P. Barkey, R. H. Muller, and C. W. Tobias, "Roughness Development in Metal Electrodeposition," J. Electrochem. Soc., **136** (8), 2199-2214, 1989.
15. R. F. Probstein, *Physicochemical Hydrodynamics: An Introduction*, Second Edition, John Wiley & Sons, Inc., New York, 1994.
16. W. C. Grande and J. B. Talbot, "Electrodeposition of Thin Films of Nickel-Iron: II. Modeling," J. Electrochem. Soc., **140** (3), 675-681, 1993.
17. S. Hessami and C. W. Tobias, "A Mathematical Model for Anomalous Codeposition of Nickel-Iron on a Rotating Disk Electrode," J. Electrochem. Soc., **136** (12), 3611-3616, 1989.
18. T. Krause, L. Arulnayagam, and M. Pritzker, "Model for Nickel-Iron Alloy Electrodeposition on a Rotating Disk Electrode," J. Electrochem. Soc., **144** (3), 960-969, 1997.
19. L. R. Petzold, "A Description of DASSL: A differential/Algebraic System Solver, SAND82-8637, Sandia National Laboratories, Livermore, CA, September 1982.
20. J. Horkans, "On the Role of Buffers and Anions in NiFe Electrodeposition," J. Electrochem. Soc., **126** (11), 1861-1867, 1979.
21. M. Matlosz, "Competitive Adsorption Effects in the Electrodeposition of Iron-Nickel Alloys," J. Electrochem. Soc., **140** (8), 2272-2279, 1993.
22. P. C. Andricacos, C. Arana, J. Tabib, J. Dukovic, and L. T. Romankiw, "Electrodeposition of Nickel-Iron Alloys," J. Electrochem. Soc., **136** (5), 1336-1340, 1989.
23. M. Ramasubramanian, S. N. Popova, B. N. Popov, R. E. White, and K. M. Yin, "Anomalous Codeposition of Fe-Ni Alloys and Fe-Ni-SiO2 Composites Under Potentiostatic Conditions," J. Electrochem. Soc., **143** (7), 2164-2172, 1996.
24. D. Gangisingh and J. B. Talbot, "Anomalous Electrodeposition of Nickel-Iron," J. Electrochem. Soc., **138** (12), 3605-3611, 1991.
25. W. C. Grande and J. B. Talbot, "Electrodeposition of Thin Films of Nickel-Iron," J. Electrochem. Soc., **140** (3), 669-674, 1993.
26. H. Dahms and I. M. Croll, "The Anomalous Codeposition of Iron-Nickel Alloys," J. Electrochem. Soc., **112** (8), 771-775, 1965.
27. D. Baudrand, *Metal Finishing*, p. 16, July, 1996.
28. R. A. F. Hammond, "Nickel Plating from Sulfamate Solutions", International Nickel Co., Ltd., monograph, 1964.
29. N. Isaev and J. G. Osteryoung, "Thermoconvection-Enhanced Deposition of Copper," J. Electrochem. Soc., **142** (12), 4103-4107, 1995.
30. K. G. Jordan and C. W. Tobias, "Simulation of the Role of Convection in Electrodeposition into Microscopic Trenches," J. Electrochem. Soc., **138** (7), 1933-1939, 1991.

31. K. Bade, K. Leyendecker, A. Thommes, W. Bacher, "Electroplating at High Aspect Ratio Micropatterned Electrodes - Influence of Mass Transfer" Proc. Fourth Intl. Symposium on Magnetic Materials, Processes, and Devices, Electrochemical Society Fall Meeting, 1995.
32. J. J. L. Higdon, "Stokes Flow in Arbitrary Two-Dimensional Domains: Shear Flow over Ridges and Cavities," J. Fluid Mech., **159**, 195-226, 1985.
33. B. J. Gebhart, Y. Jaluria, R. L. Mahajan, and B. Sammakia, *Bouyancy-Induced Flows and Transport: Textbook Edition*, Hemisphere Publishing Corporation, New York, 1988.
34. R. C. Alkire, H. Deligianni, and J. B. Ju, "Effect of Fluid Flow on Convective Transport in Small Cavities," J. Electgrochem. Soc., **137** (3), 818-824, 1990.
35. H. K. Kuiken, "Etching: a Two-Dimensional Mathematical Approach," Proc. R. Soc. Lond., **A392**, 199-225, 1984.
36. H. K. Kuiken,"Etching Through a Slit," Proc. R. Soc. Lond, **A396**, 95-117, 1984.
37. M. Georgiadou and R. Alkire, "Anisotropic Chemical Pattern Etching of Copper Foil," J. Electrochem. Soc., **141** (3), 675-689, 1994.
38. A. K. Prasad and J. R. Koseff, "Combined Forced and Natural Convection Heat Transfer in a Deep Lid-Driven Cavity Flow," Int. J. Heat and Fluid Flow, **17**, 460-467, 1996.
39. G. de Valh Davis, E. Leonardi, and M. P. van Schie, "Three-Dimensional Natural Convection in a Cavity with Localized Heating and Cooling," University of South Wales Report 1988/FMT/5, June 1988.
40. J. N. Reddy and A. Satake, "A Comparison of a Penalty Finite Element Model with the Stream Function-Vorticity Model of Natural Convection in Enclosures," J. Heat Trans., **102**, 659-666, 1980.
41. H.Q. Yang, K.T. Yang, and J. R. Lloyd, "Three-dimensional bimodal buoyant flow transitions in tilted enclosures," Int. J. Heat and Fluid Flow, **9** (2), 90-97, 1988.
42. R. J. Goldstein and S. Tokuda, "Heat Transfer by Thermal Convection at High Rayleigh Numbers" Intl. J. Heat Mass Trans., **23**, 738-740, 1980.

Related Reading

1. R. A. Tacken, L. J. J. Janssen, "Applications of Magnetoelectrolysis,"J. Appl. Electrochem., **25**, 1-5, 1995.
2. J. Fujioka, "A Mathematical Model for Electrocrystallization under Linear Sweep Voltammetry Conditions," Journal of Crystal Growth, **91**, 147-154, 1988.
3. P. H. Vallotton, M. Matlosz, D. Landolt, "Experimental investigation of the terminal effect in lead electrodeposition onto resistive substrates" J. Appl. Electrochem., **23**, 927-932, 1993.
4. C. G. Law, Jr., and J. Newman, 'Corrosion of a Rotating Iron Disk in Laminar, Transition, and Fully Developed Turbulent Flow," J. Electrochem. Soc., **133** (1), 37-42, 1986.

5. B. N. Popov, K.-M. Yin, and R. E. White, "Galvanostatic Pulse and Pulse Reverse Plating of Nickel-Iron Alloys from Electrolytes Containing Organic Compounds on a Rotating Disk Electrode," J. Electrochem. Soc., **140** (5), 1321-1330, 1993.
6. J. O. Dukovic, "Computation of Current Distribution in Electrodeposition, A Review," IBM J. Res. Develop., **34** (5), 693-705, 1990.
7. D. A. Hazelbeck and J. B. Talbot, "Modeling of Additive Effects on the Electroplating of a Through-Hole," AIChE Journal, **36** (8), 1145-1155, 1990.
8. J. Horkans, "Effect of Plating Parameters on Electrodeposited NiFe," J. Electrochem. Soc., **128** (1), 45-49, 1981.
9. S. Roy, M. Matlosz, and D. Landolt, "Effect of Corrosion on the Composition of Pulse-Plated Cu-Ni Alloys," J. Electrochem. Soc., **141** (6), 1509-1516, 1994.
10. T. M. Harris and J. St. Clair, "Testing the Role of Metal Hydrolysis in the Anomalous Electrodeposition of Ni-Fe Alloys," J. Electrochem. Soc., **143** (12), 3918-3922, 1996.
11. G. H. Bernstein, D. A. Hill, and W.P. Liu, "New High-Contrast Developers for Poly(methyl methacrylate) Resist," J. Appl. Phys., **71** (8), 4066-4075, 1992.
12. W. J. Cooper, P. D. Krasicky, and F. Rodriguez, "Dissolution Rates of Poly(Methyl Methacrylate) Films in Mixed Solvents," J. Appl. Polymer Sci., **31**, 65-73, 1986.
13. E. E. Parsonage, N. A. Peppas, and P. I. Lee,"Properties of Positive Resists - II: Dissolution Characteristics of Irradiated Poly(methyl methacrylate) and Poly(methyl methacrylate-co-maleic anhydride)," J. Vac. Sci. Technol., **B5** (2) 538-545, 1987.
14. N. A. Peppas, J. C. Wu, and E. D. von Meerwall, "Mathematical Modeling and Experimental Characterization of Polymer Dissolution," Macromolecules, **27**, 5626-5638, 1994.
15. F. Penot, "Numerical Calculation of Two-Dimensional Natural Convection in Isothermal Open Cavities," Numerical Heat Transfer, **5**, 421-437, 1982.
16. N. K. Ghaddar, M. Magen, B. B. Mikic, and A. T. Patera, "Numerical invewtigation of incompressible flow in grooved channels. Part 2. Resonance and oscillatory heat-transfer enhancement," J. Fluid Mech., **168**, 541-578, 1986.
17. R. Alkire and H. Deligianni, "The Role of Mass Transport on Anisotropic Electrochemical Pattern Etching," J. Electrochem. Soc., **135** (5), 1093-1100, 1988.
18. J. M. Occhialini and J. J. L. Higdon, "Convective Mass Transport from Rectangular Cavities in Viscous Flow," J. Electrochem. Soc., **138** (10), 2845-2855, 1992.
19. J. O'M. Bockris and A. K. N. Reddy, *Modern Electrochemistry, Vols. 1 and 2,* Plenum Press, New York, 1970.
20. F. A. Lowenheim ed., *Modern Electroplating*, Wiley-Interscience, 1974.
21. F. A. Lowenheim, *Electroplating*, McGraw Hill, New York, 1978.
22. E. Gileadi,*Electrode Kinetics for Chemists, Chemical Engineers, and Scientists*, VCH Publishers, New York, 1993.

UNLIMITED RELEASE
INITIAL DISTRIBUTION

0961 J. A. Sayre, 1403
1434 G. E. Pike, 1802
1411 D. B. Dimos, 1831
0481 K. D. Meeks, 2167
0329 D. W. Plummer, 2643
Attn: T. R. Christenson, 2643
A. D. Oliver, 2643
E. J. Garcia, 2643
0149 C. E. Meyers, 4000
9001 T. O. Hunter, 8000
Attn: M. E. John, 8100
L. A. West, 8200
R. C. Wayne, 8400
D. L. Crawford, 8900
9403 M. A. Bankert, 8230
9403 D. R. Boehme, 8230
9403 W. D. Bonivert, 8230
9403 J. T. Hachman, 8230
9403 J. M. Hruby, 8230
9403 A. M. Morales, 8230
9403 M. X. Tan, 8230
9054 W. J. McLean, 8300
Attn: W. Bauer, 8358
D. R. Hardesty, 8361
L. A. Rahn, 8351
F. P. Tully, 8353
R. W. Carling, 8362
9041 J. S. Binkley, 8345
9042 G. H. Evans, 8345
9042 S. K. Griffiths, 8345 (5)
9042 A. Ting, 8345
9042 R. S. Larson, 8345
9042 R. H. Nilson, 8345
9056 P. H. Paul, 8351
9405 T. M. Dyer, 8700
Attn: C. M. Hartwig, 8701
M. I. Baskes, 8712
G. J. Thomas, 8715
K. L. Wilson, 8716
S. M. Foiles, 8717
9904 W. D. Wilson, 8700
9403 J. C. F. Wang, 8713
9403 R. W. Bradshaw, 8713
0841 P. J. Hommert, 9100

9018 Central Technical Files, 8940-2 (3)
0899 Technical Library, 4916 (4)
9021 Technical Communications Dept., 8815/
Technical Library, MS 0899, 4916
9021 Technical Communications Dept., 8815
for DOE/OSTI, 8815 (2)